CHAPTER 5

SYNTHESIS AND TRIBOLOGICAL CHARACTERIZATION OF Cu- (2 wt. %)rGO-MoS_2 HYBRID COMPOSITES

This chapter begins with the results on the characterization raw powders of rGO, MoS_2, and synthesized rGO-MoS_2 hybrid, this is followed by the microstructure and properties (physical and mechanical) evaluation of Cu-2.0 wt. % rGO-MoS_2 composites prepared at different sintering temperatures of 600, 650, 700, and 750 $^{\circ}$C. The friction and wear tests have been conducted at a fixed load of 4 N and a sliding speed of 0.5 $m.s^{-1}$ against steel ball for the composites and pure Copper (PC). The primary focus of the study is to determine the optimum sintering temperature for the fabrication of composite with optimum friction and wear characteristics under given conditions of dry sliding and to examine the effect of load on the tribological performance of the optimised composite. Finally, the results have been discussed to understand the role of load as well as the tribo-events that take place during sliding.

5.1 RESULTS

5.1.1 CHARACTERIZATIONS OF SYNTHESIZED POWDERS (rGO, MoS_2, and rGO-MoS_2)

This section contains the characterization of synthesized powders like rGO, MoS_2, and hybrid material rGO-MoS_2, which have been used as a reinforcement for fabricating the Cu-based composites.

Figure 5.1 presents the microstructures of rGO and MoS_2, as examined under TEM and HR-TEM. The low and the high magnification TEM micrographs of rGO given in Figs. 5.1 (a) and (b), respectively, and HRTEM image of rGO shown in the inset of Fig. 5.1 (b) reveal the presence of multi-layered reduced graphene sheets having few wrinkles. Figures 5.1 (c) and (d) show the microstructure of MoS_2 powder at low and high magnifications, respectively, whereas the inset given in Fig 5.1 (d) corresponds to the HRTEM image of MoS_2. One may observe the presence of several MoS_2 nano ribbons in TEM images, which appear to be entangled together, however, a stacked-layer structure of MoS_2 could be seen in the HRTEM image given in the inset.

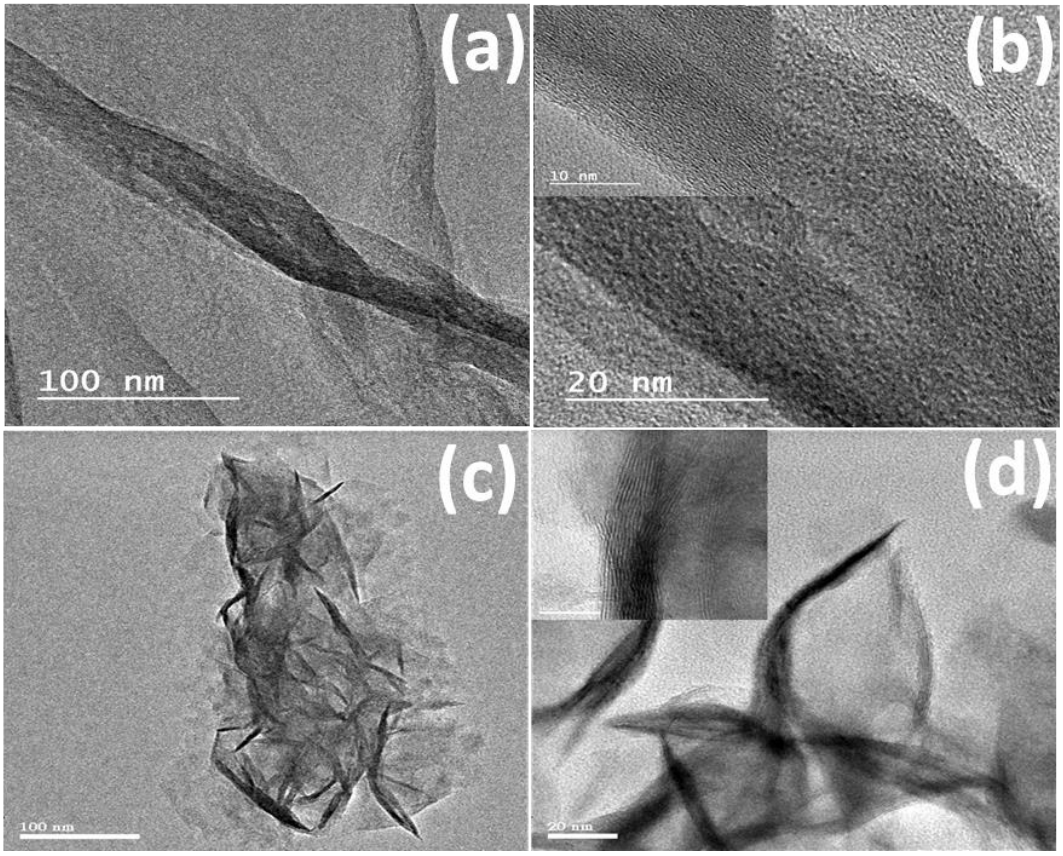

Fig. 5.1 TEM micrographs correspond to a low and high magnification of a-b) rGO, c-d) MoS_2. The inset of the micrographs (b and d) corresponds to the HRTEM image of respective nanoparticles.

The microstructural features of rGO-MoS_2 hybrid examined under TEM and presented in Fig. 5.2 (a) clearly demonstrates the growth of MoS_2 nanosheets on the rGO skeleton, as indicated by white arrows. The ribbon-like structures of MoS_2 having 100-200 nm length with 8-15 molecular lamellae homogeneously grown on the rGO could be observed in Fig. 5.2 (b). The rGO lamellae having a lateral dimension in the range of few microns may also be seen in the HRTEM image given in the inset in Fig. 5.2 (b). The inter-lamellar spacing, as highlighted in the inset of Fig. 5.2 (b) is found to be 0.63 nm, which is very close to the characteristics interlayer spacing of 0.616 nm for MoS_2 nanosheets. Figure 5.2 (c) shows the TEM image of rGO-MoS_2 along with corresponding elemental distribution of Mo, S, and C. The uniform distribution of Mo and S beside the C in rGO-MoS_2 hybrid nanosheets points towards a homogeneous distribution of MoS_2 nanosheets in the rGO-MoS_2 hybrid.

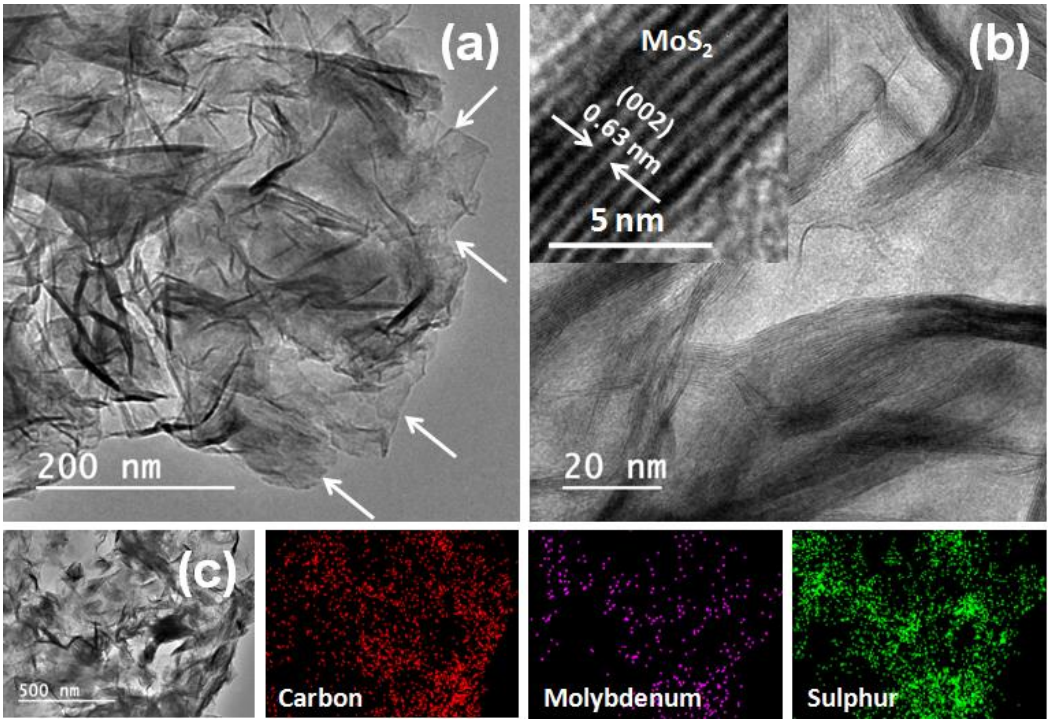

Fig. 5.2 Illustration of low and high-resolution micrographs of rGO-MoS_2 hybrid captured by TEM. (a) The rGO lamellae are indicated by white arrows in figure (b), whereas MoS_2 lamellae are explicitly shown in figure (b) with interlamellar spacing and (c) Microscopic image along with corresponding area elemental distribution of C, Mo, and S in the rGO-MoS_2 hybrid.

The survey spectrum of rGO-MoS_2 hybrid as examined under XPS and given in Fig. 5.3 (a), explicitly exhibits characteristic features owing to constituents (rGO and MoS_2) of the rGO-MoS_2 hybrid. The high-resolution C 1s, Mo 3d, and S 2p spectra of rGO-MoS_2 hybrid shown in Fig. 5.3 (b) are deconvoluted to understand their chemical nature and bonding patterns. The C 1s peak centered at 284.6 eV could be deconvoluted into three peak components at 284.6, 286.1, and 288.3 eV assigned to C=C/C-C, C-O, and COOH groups, respectively. A deconvoluted peak at 284.6 with a major fraction of total intensity suggests the abundance of C=C and C-C carbons in the rGO of rGO-MoS_2 hybrid. The presence of residual oxygen functionalities (viz. hydroxyl, phenolic, ether, ketonic, carboxylic, etc.) manifested in the form of peak components at higher binding energies at 286.1 and 288.3 eV. The Mo 3d shows a doublet peak centered at 229.6 and 232.8 eV corresponding to Mo $3d_{5/2}$ and Mo $3d_{3/2}$, respectively. The peak-spacing of 3.2 eV due to the spin-orbit splitting of 3d reveals the +4 oxidation state of Mo in the rGO-MoS_2 hybrid. The XPS peaks at binding energies of 162.4, 163.6, and 226.9 eV may be ascribed to S $2p_{3/2}$, S $2p_{1/2,}$ and S 2s orbits, respectively, of MoS_2 in the rGO-MoS_2 hybrid. The weak shoulder of Mo 3d at a higher binding energy of 236.3 eV is assigned to the Mo (VI) oxidation state, and the same may be attributed to the presence of traces of MoO_3 in the rGO-MoS_2 hybrid.

The XRD pattern of rGO-MoS_2 hybrid shown in Fig. 5.4, demonstrates the crystalline features while exhibiting the characteristic diffractions at 2θ of 13.9º, 33.3º, 39.3º, and 58.9º corresponding to the (002), (101), (103), and (110) planes of MoS_2 nanosheets as per the JCPDS card no. 37-1492. The (002) plane at 2θ of 13.9° represents the interlamellar spacing of 0.637 nm in the MoS_2 nanosheets of the rGO-MoS_2 hybrid. The XRD pattern also displays comparatively weak and broad diffraction at 2θ of 24.8º corresponding to the (002) plane of graphene with an interlamellar spacing of 0.358 nm.

These characteristics diffraction features confirm the successful preparation of rGO-MoS_2 hybrid. The first-order Raman spectrum of rGO-MoS_2 hybrid shown in Fig. 5.5 reveals D and G bands suggesting the presence of structural defects and sp^2 carbon domains, respectively, in the graphene skeleton. During the hydrothermal treatment, a major fraction of oxygen functionalities in the GO gets eliminated and yields the rGO. Simultaneously, the structural defects and residual oxygen functionalities act as active sites for the synthesis of MoS_2 under the hydrothermal reaction. The higher intensity ratio (I_D:I_G = 1.39) between the D and G bands indicates the existence of structural defects and distortions in the graphene lamellae of rGO-MoS_2 hybrid. The presence of MoS_2 could be confirmed by characteristic A_{1g} band at 403 cm^{-1}, which is shown in the inset of Fig. 5.5.

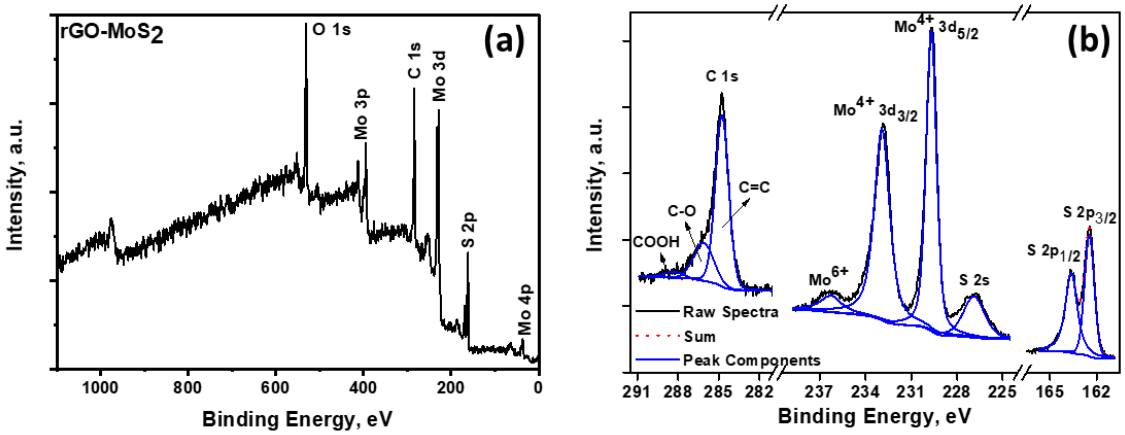

Fig. 5.3 (a) XPS spectrum of rGO-MoS_2 hybrid and (b) XPS spectra of C 1s, Mo 3d, and S 2p along with their deconvoluted peak components.

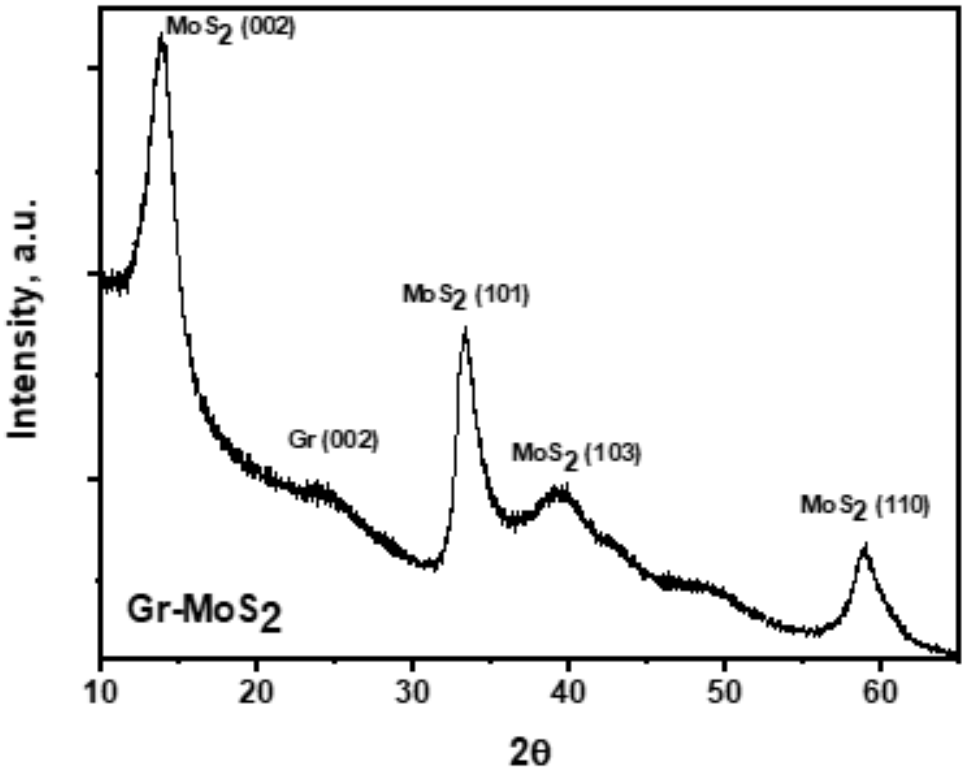

Fig. 5.4 XRD pattern of rGO-MoS_2 hybrid.

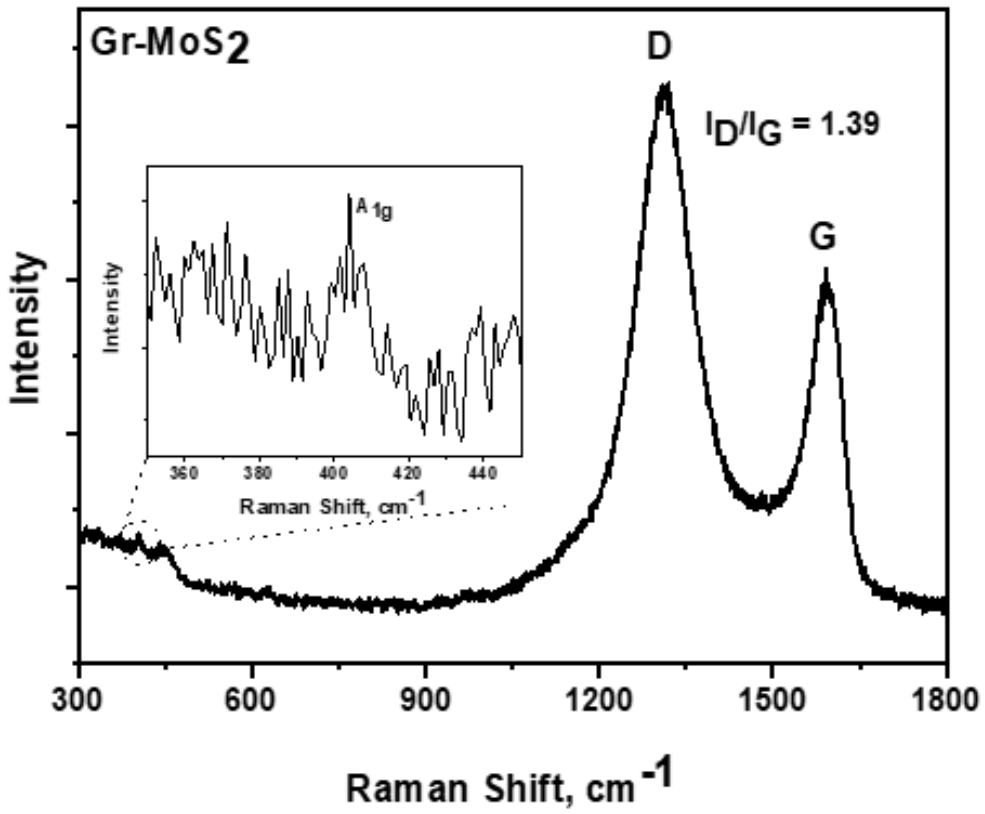

Fig. 5.5 Raman band A_{1g} of MoS_2 nanosheets in the rGO-MoS_2 hybrid.

5.1.2 CHARACTERIZATION OF THE SYNTHESIZED COMPOSITES

Figures 5.6 (a through d) show the backscattered SEM micrographs of Cu based composites containing a fixed amount (2 wt. %) rGO-MoS_2 and sintered at different temperatures of 600 (designated as CGM 600), 650 (designated as CGM 650), 700 (designated as CGM 700) and 750 $^{\circ}$C (designated as CGM 750). All the composites have been observed to exhibit similar microstructural features, wherein dark spots correspond to rGO rich regions, and bright areas correspond to the MoS_2 rich region. One may observe an increase in the dark phase with increasing sintering up to 700 $^{\circ}$C followed by a decrease with an increase in the temperature to 750 $^{\circ}$C.

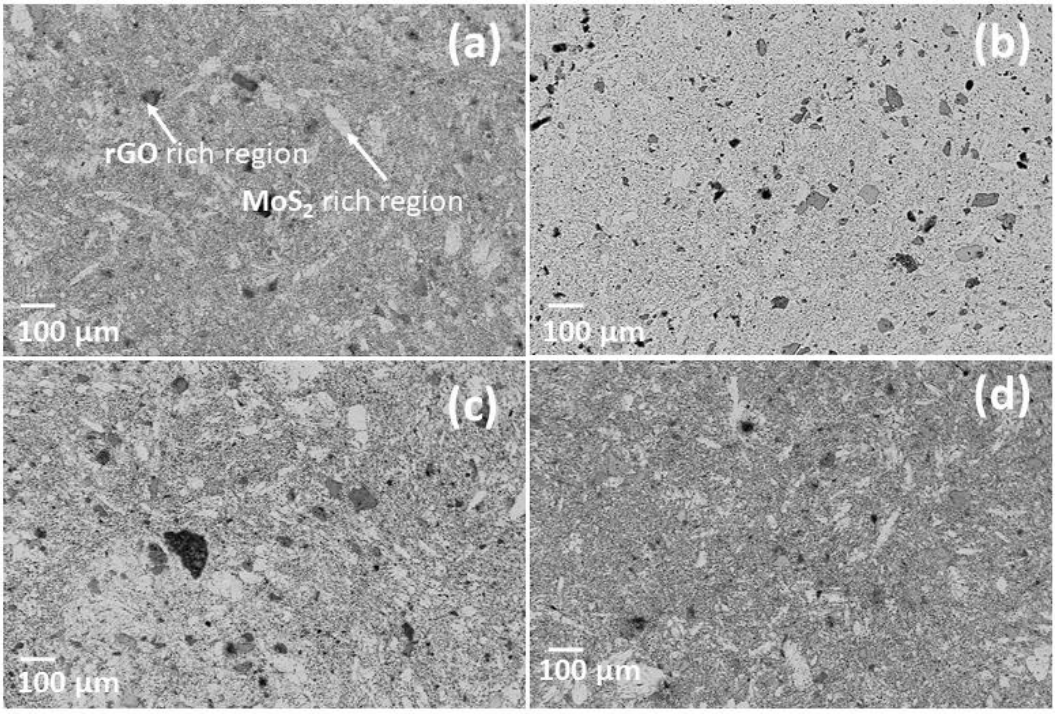

Fig. 5.6 Back-scattered mode SEM micrograph of Cu-rGO-MoS_2 (a) CGM 600, (b) CGM 650, (c) CGM 700, (d) CGM 750, prepared at sintering temperatures of 600, 650 and 700 and 750 $^{\circ}$C, respectively.

In order to have an in-depth microscopic understanding, the microstructure of CGM 700 composite has further been examined under TEM and HRTEM. Figures 5.7 (a and b) show the bright field TEM images of Cu-2.0 wt. % rGO-MoS_2 (CGM 700)

composite fabricated at a sintering temperature of 700 ˚C. One may clearly observe the well dispersed rGO-MoS_2 hybrid nanoparticles in the copper matrix (marked with black arrows) in the TEM micrograph of the composite shown in Fig. 5.7 (a). The lattice fringes are explicitly seen in Fig. 5.7 (b) and the lack of distinct boundaries between the rGO-MoS_2 hybrid of 2-5 nm size and copper matrix point towards the multilateral interactions or linkages between the matrix and the reinforcement. The selected area diffraction pattern shown in Fig. 5.7 (c) illustrates the crystalline features of Cu-rGO-MoS_2 composite by demonstrating the characteristics rings owing to Cu (111), MoS_2 (002), MoC (103), and rGO (002) planes. HRTEM micrograph shown in Fig. 5.6 (d) depicts the moire pattern lattice fringes, which confirms the coexistence of two phases and good interfacial bonding between the matrix and the reinforcement phase. The interface between the copper matrix and rGO-MoS_2 particle is shown in the micrograph with the help of white arrows.

X-ray diffraction patterns of Cu-2.0 wt. % rGO-MoS_2 composites sintered at different temperatures of 600, 650, 700 and 750 ˚C i.e. CGM 600, CGM 650, CGM 700 and CGM 750 shown in Fig. 5.8 exhibit two intense diffraction peaks of Cu at 2θ of 43.3, and 50.4° corresponding to (111) and (200) planes. These planes suggest the FCC structure of the copper matrix as per the JCPDS card no. 85-1326. Further, no significant difference could be observed in any of the diffraction patterns with respect to sintering temperature, as evident from Figs. 5.8 (a to d). The XRD features owing to rGO-MoS_2 hybrid in the composite specimens have poor intensity. Hence, they are expanded in the inset figures to reveal their characteristic features. The presence of rGO is confirmed by a characteristic diffraction peak at 2θ of 26.5° owing to (002) plane. A broad XRD peak at 2θ of 33.4° corresponding to the (101) plane suggests the presence of MoS_2 in the Cu-rGO-MoS_2 composites. A new diffraction peak at 2θ of 36.4°, corresponds to (111) plane of molybdenum carbide (MoC) as per the JCPDS card no.89-2868 is also observed.

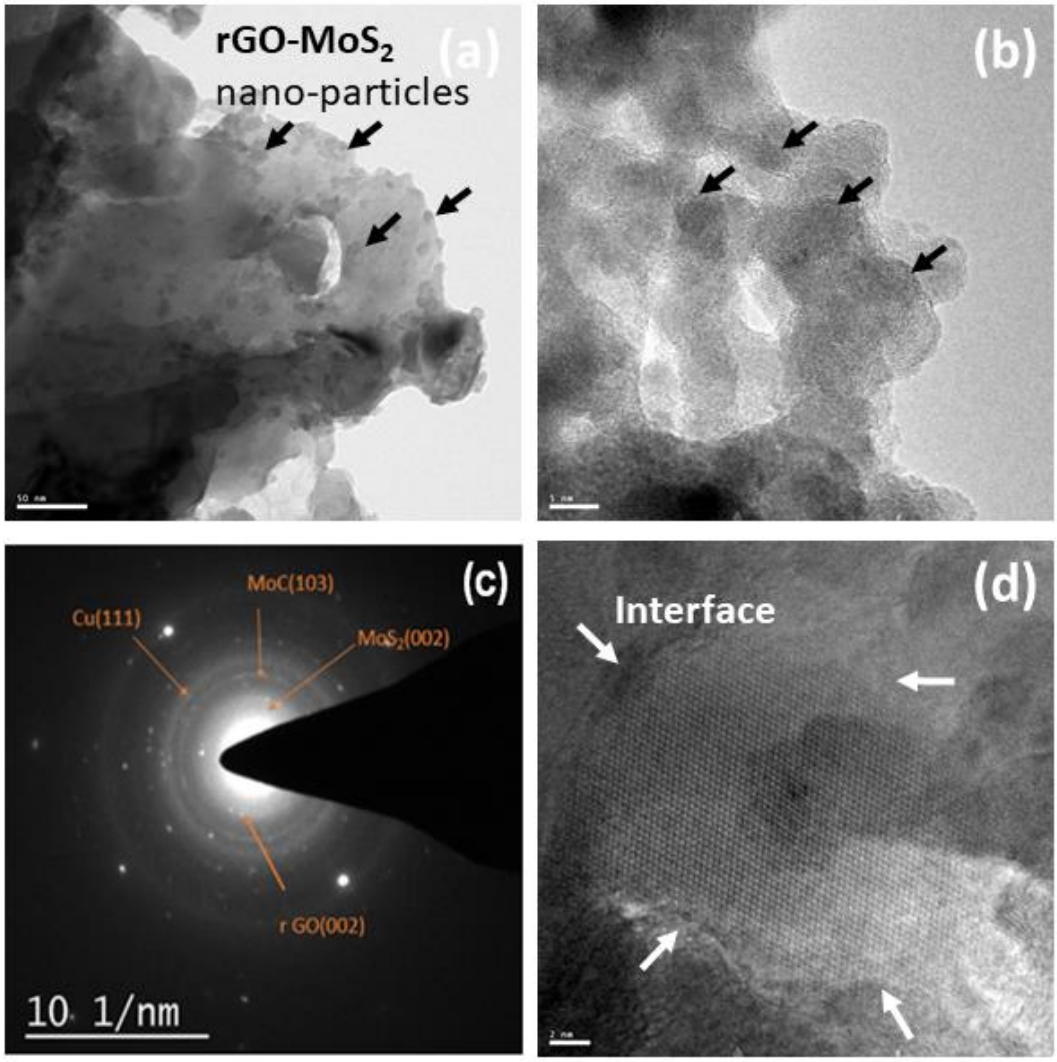

Fig. 5.7 (a-b) TEM micrograph of Cu-rGO-MoS_2 composite (c) Selected area diffraction pattern of Cu-rGO-MoS_2 composite (d) HRTEM micrograph showing the interface of copper and rGO-MoS_2 phase.

Raman spectra of composites sintered at different temperatures are shown in Fig. 5.9. Figure 5.9 (a) shows the ratio of sp^3 to sp^2 hybridization, i.e. I_D:I_G ratio with respect to sintering temperature. No noticeable change could be observed in I_D:I_G ratio with respect to sintering temperature, and the ratio is around 1.20. It is confirmed from the intensity ratio that, after the composite synthesis, GO remains in the reduced graphene form, despite a reduction in I_D:I_G ratio from 1.39 to 1.20. Raman shift in G peak position shown in Fig. 5.13(b) indicates a blue shift in the G peak with an increase in temperature up to 700 $^{\circ}$C, which is followed by a redshift for 750 ^{0}C.

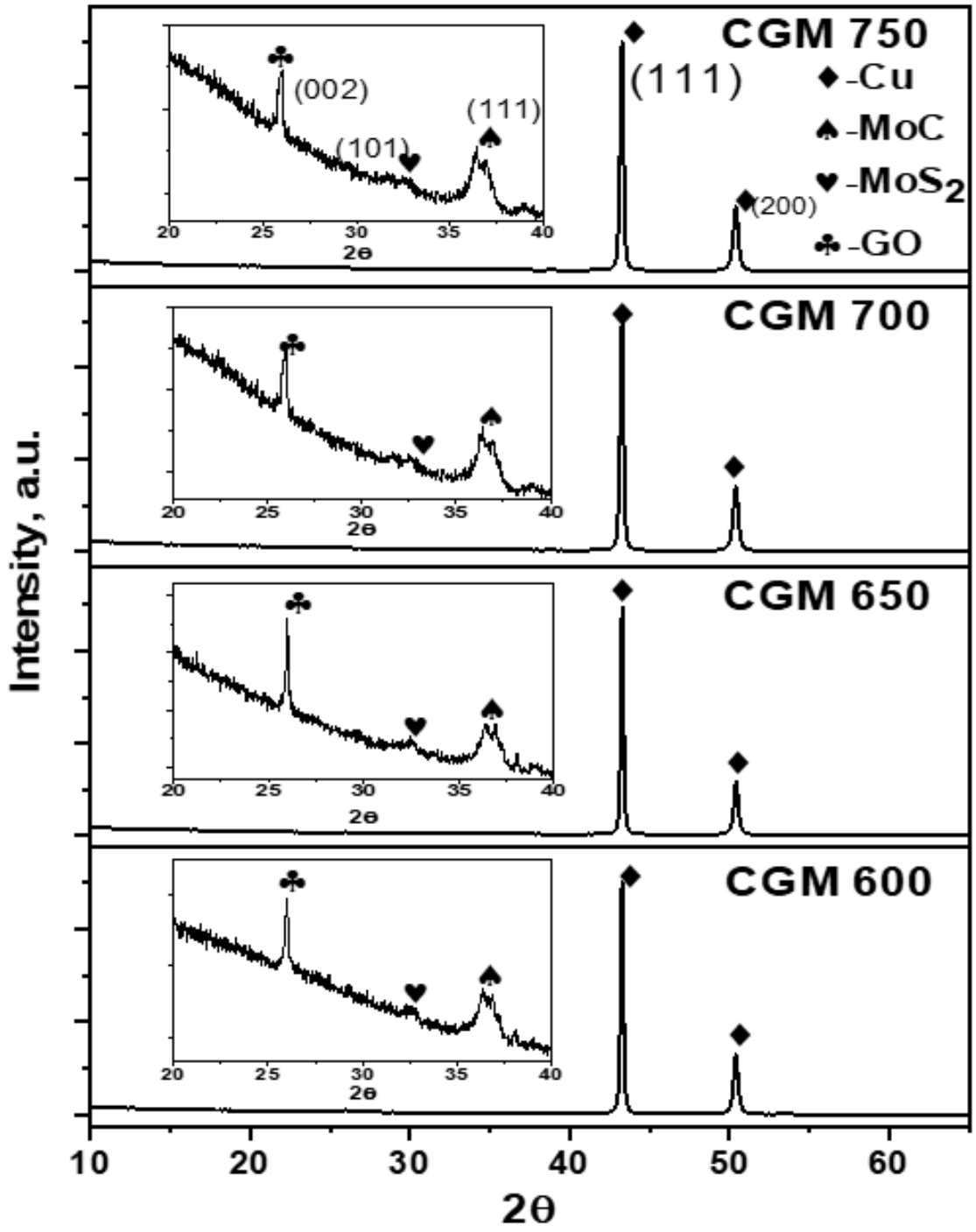

Fig. 5.8 XRD patterns of CGM 600, CGM 650, CGM 700, and CGM 750 specimens. The characteristics features due to rGO, MoS_2, and MoC are expanded in their inset graphs.

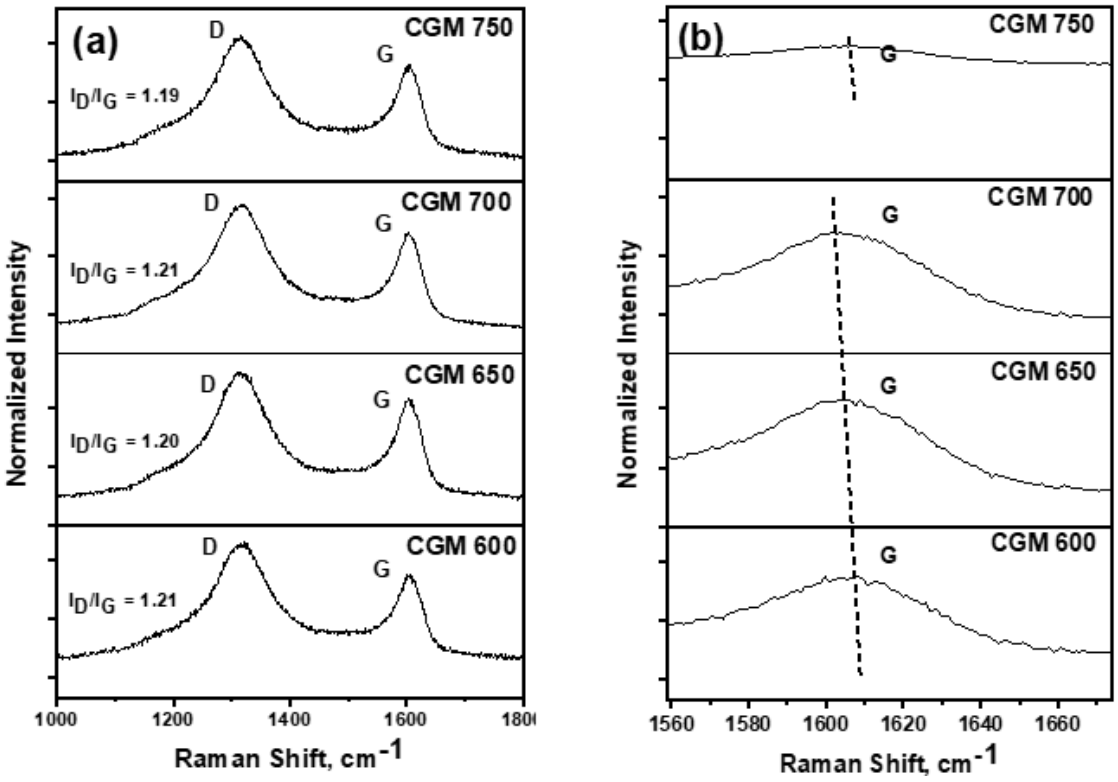

Fig. 5. 9 (a) Raman spectra of Cu-rGO-MoS_2 composites prepared at sintering temperature of 600 ˚C, 650 ˚C, 700 ˚C, and 750 ˚C. The G and D bands revealed the presence of rGO in Cu-rGO-MoS_2 composites. (b) Shift in G peak position with sintering temperature.

5.1.3 PHYSICAL AND MECHANICAL PROPERTIES OF COMPOSITES

Figure 5.10 shows the punch displacement *vs.* sintering temperature profiles for CGM 600, CGM 650, CGM 700, and CGM 750 composites. The punch displacement exhibits a decreasing (negative) trend after 425 ˚C, as seen from the profiles, and becomes more negative with increasing sintering temperature. The least negative punch displacement is observed for composite, CGM 600, sintered at 600 ˚C, whereas the greatest displacement is observed for CGM 750 sintered at a temperature of 750 ˚C.

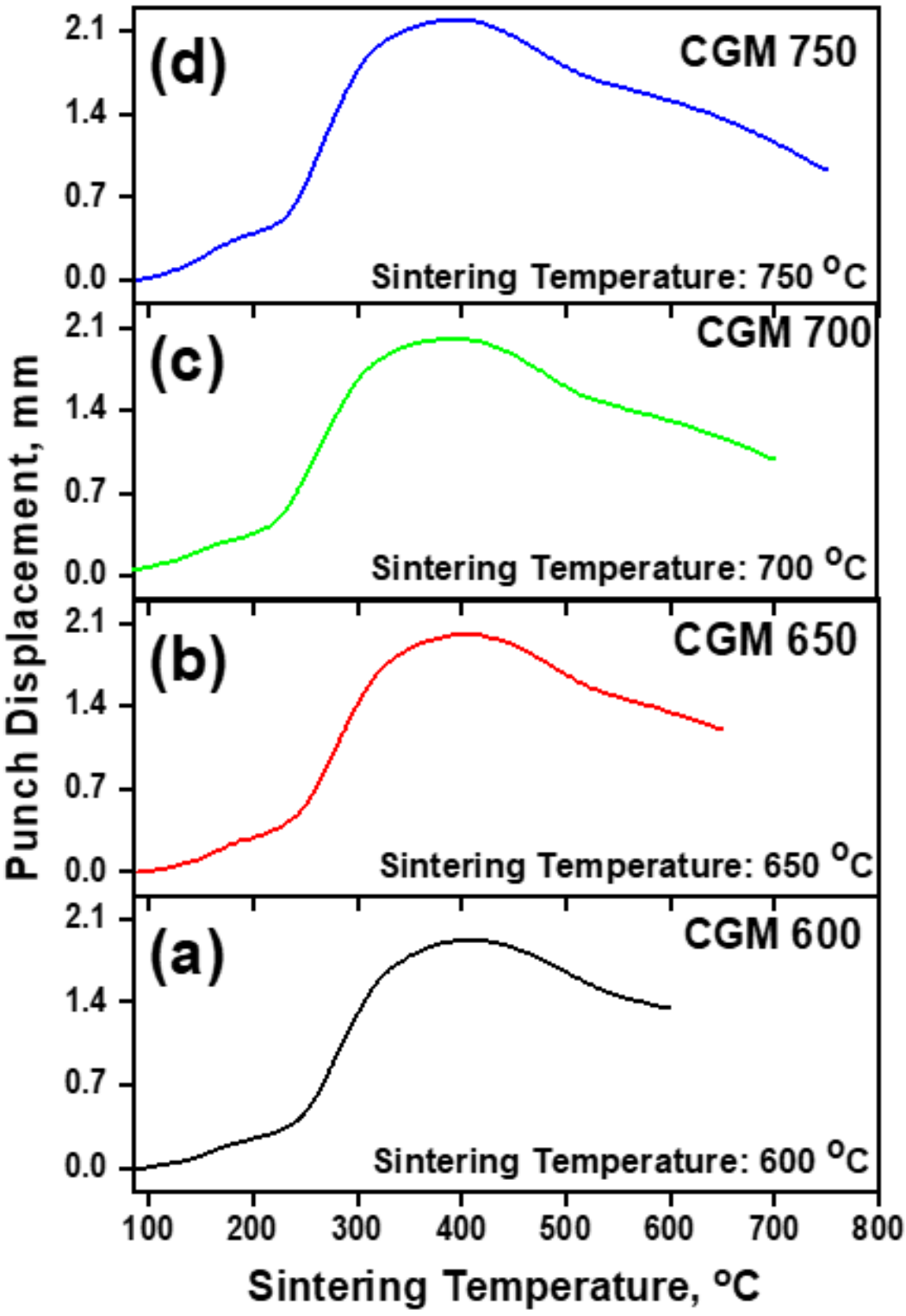

Fig. 5.10 Variation of punch displacement with sintering temperature.

The density of the composites sintered at different temperatures has been estimated by the Archimedes principle, hardness has been measured using hardness tester,

and the mechanical properties have been found by carrying out the tensile testing. Table 5.1 presents the density, hardness, yield strength, ultimate tensile strength, and % elongation of pure copper (PC) and Cu-rGO-MoS_2 composites synthesized at different sintering temperatures. The pure copper (PC) specimen chosen as a reference material has also been synthesized through spark plasma sintering. The density and the hardness of pure Cu are found to be 8.434 $g.cm^{-3}$ and 53 HV, respectively. The density of copper is found to decrease in adding 2 wt. % of rGO-MoS_2 hybrid, whereas the hardness is found to increase as evident from Table 5.1. Further, one may also observe a decrease in both the density and the hardness of composites with increasing temperature of sintering. Figure 5.12 displays the tensile strain-stress curves of CGM 600. CGM 650, CGM 700, and CGM 750 composites, which exhibit three regions; (a) elastic pattern up to yield point, (b) strain hardening, and (c) elongation between ultimate tensile strength (UTS) and the fracture. The Cu-rGo-MoS_2 composite prepared at sintering temperature of 600 $^{\circ}$C has shown the maximum UTS (121 MPa) and % elongation among all the composites, as illustrated in Table 5.1. The UTS is observed to decrease with increasing sintering temperature. However, % elongation is found to decrease with an increase in the sintering temperature from 600 to 700 $^{\circ}$C followed by an increase for 750 $^{\circ}$C.

Table 5.1 Physical and mechanical properties of synthesized copper and composites.

Specimen	**Density, $g.cm^{-3}$**	**Hardness, $HV_{0.5}$**	**Yield Strength, MPa**	**UTS, MPa**	**% Elongation**
PC	8.434	53	-	-	-
CGM 600	7.652	84	91.19	120.77	4.32
CGM 650	7.593	79	94.71	118.56	3.96
CGM 700	7.514	72	93.98	117.23	3.92
CGM 750	7.501	70	86.03	110.87	4.31

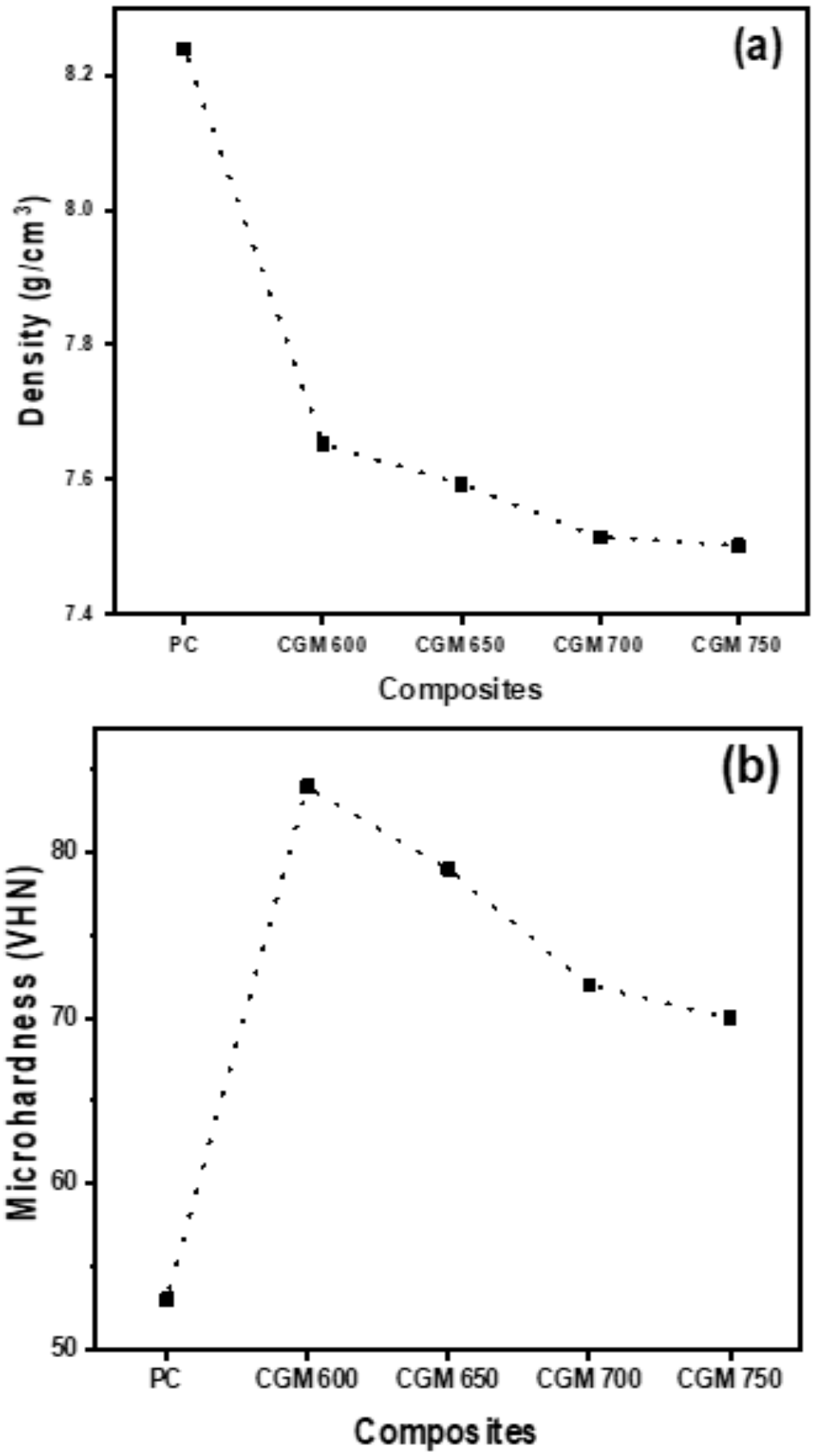

Fig. 5.11 Variation of (a) Density and (b) Hardness with composites.

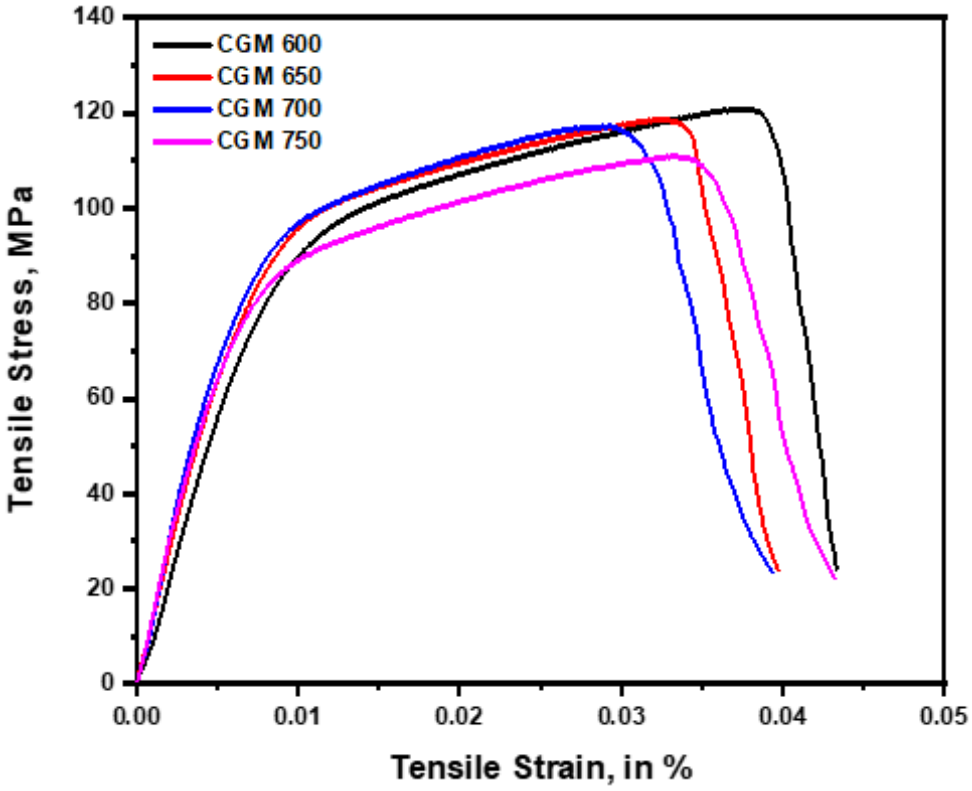

Fig. 5.12 Tensile stress-strain curve for specimen sintered at different temperatures.

Figures 5.13 (a through d) show the fractured surfaces of different composites as examined under SEM along with their elemental mapping illustrating the distribution of Cu, C, Mo and S. One may observe the presence of dimples, characteristics of a ductile mode of failure in the micrographs of all of the composites. However, the dimples appear to be relatively shallow in the composite sintered at a relatively higher temperature. Also, relatively fewer dimples are observed for the composite fabricated at relatively higher sintering temperatures of 700 and 750 $^{\circ}$C. Elemental mapping shows the uniform distribution of C, Mo, and S for the composites sintered at relatively lower temperatures (CGM 600 and CGM 650) in comparison to those sintered at higher temperatures (CGM 700 ad CGM 750) which present non-uniform dispersion and agglomeration as evident from Figs. 5.13 (a through d).

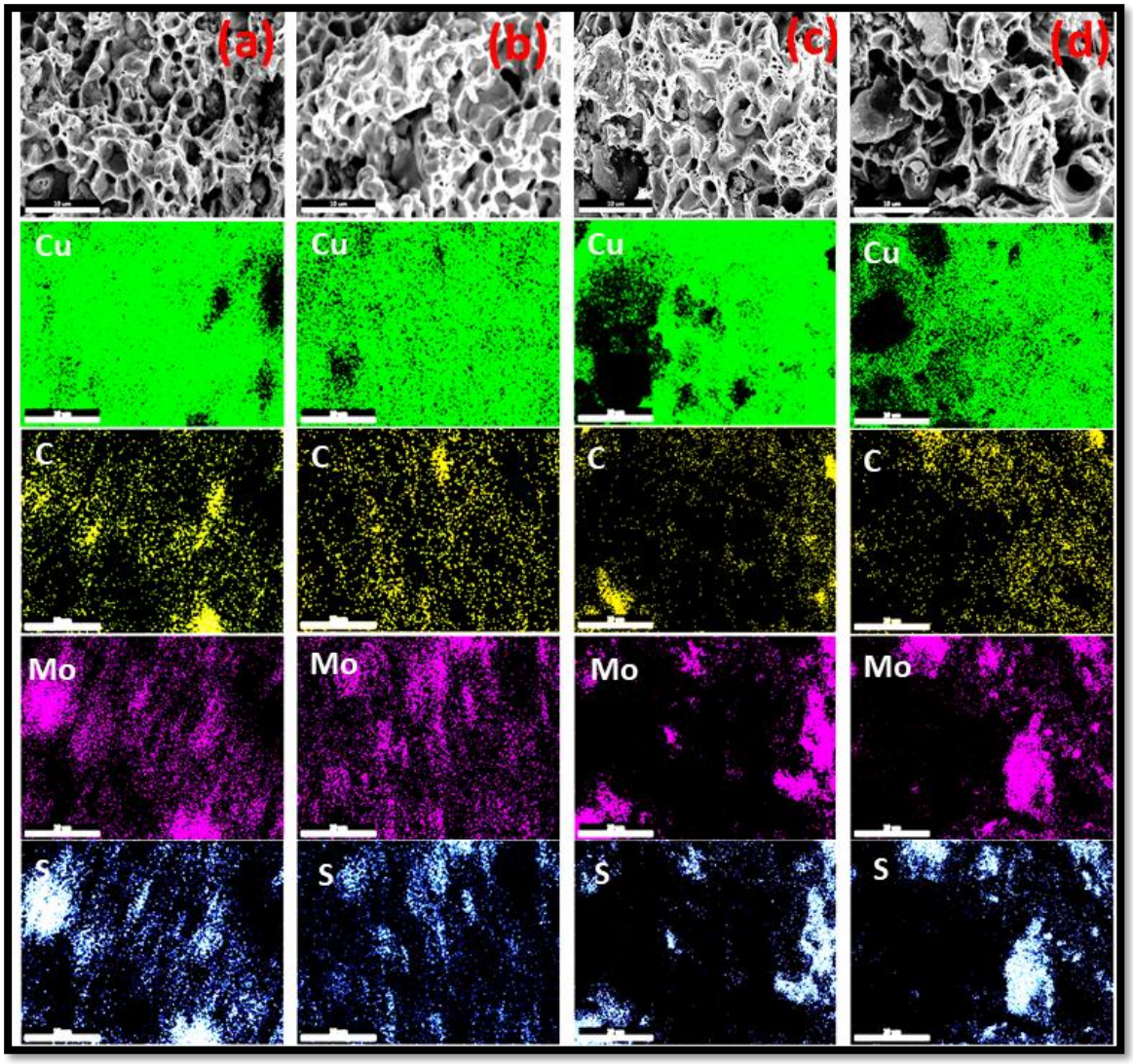

Fig. 5.13 Fractographs of composites (a) CGM 600, (b) CGM 650, (c) CGM 700, (d) CGM 750 and their corresponding elemental mapping.

5.1.4 FRICTION AND WEAR BEHAVIOR OF rGO-MoS_2 REINFORCED COMPOSITES

This section presents the results pertaining to friction and wear behavior of pure copper (PC) and copper based composites containing rGO-MoS_2 i.e. CGM 600, CGM 650, CGM 700, and CGM 750. The tests have been conducted using a ball on disc tribometer under rotary motion at a fixed load of 4 N and a sliding speed of 0.5 $m.s^{-1}$. Figure 5.14 (a) shows the variation of friction coefficient of pure Cu (PC) and Cu-rGO-MoS_2 composites with number of cycles while sliding against the steel ball as a counter

body. Pure copper has shown a high coefficient of friction ($\mu = 0.35 \pm 0.08$) with a relatively larger amplitude of fluctuations, whereas Cu-rGO-MoS_2 composites exhibit a significantly lower coefficient of friction in comparison to PC with reduced amplitude of fluctuations. Among the composites, the coefficient of friction is found to decrease with increasing sintering temperature from 600 to 700 $^{\circ}$C followed by an increase for the composite sintered at 750 $^{\circ}$C as evident from Fig. 5.14 (a). The average coefficients of friction of pure Cu as well as composites slid at a normal load of 4N and a speed of 0.5 m. s^{-1} for 6000 cycles are shown in Figure 5.14 (b). The coefficient of friction of pure Cu has been observed to reduce significantly (from 0.35 to 0.12) by adding 2 wt. % of rGo-MoS_2. Among the composites, the friction coefficient has been found to decrease gradually with increasing sintering temperature from 600 to 700 $^{\circ}$C, corresponding to CGM 600 (μ_{avg}: 0.125), CGM 650 (μ_{avg}: 0.084) and CGM 700 (μ_{avg}: 0.060). However, one may observe an increase in the average coefficient of friction (μ_{avg}: 0.107) for the composite CGM750 sintered at a temperature of 750 °C. The CGM 700 composite prepared at a sintering temperature of 700 °C has shown the lowest coefficient of friction (0.06).

Figure 5.15 depicts the variation of wear rate for pure Cu and Cu-rGO-MoS_2 composites sintered at different temperatures. A significant reduction (~35 fold) in wear rate is found to occur by the addition of rGO-MoS_2 hybrid in pure Cu, as evident from a sharp reduction in Fig. 5.15 as one move from PC to CGM 600. Copper is found to wear out at a very high wear rate (243×10^{-4} $mm^3.m^{-1}$) in comparison to the composite (6.8×10^{-4} $mm^3.m^{-1}$) than that of composites. The wear rate of the composites has been observed to decrease with increasing temperature of sintering from 600 to 700 $^{\circ}$C, which is followed by a marginal increase beyond that, as seen from Fig. 5.15. However, among the composites, the CGM 700, sintered at 700 $^{\circ}$C has shown the lowest wear rate whereas CGM 600, sintered at 600 $^{\circ}$C has the largest wear rate.

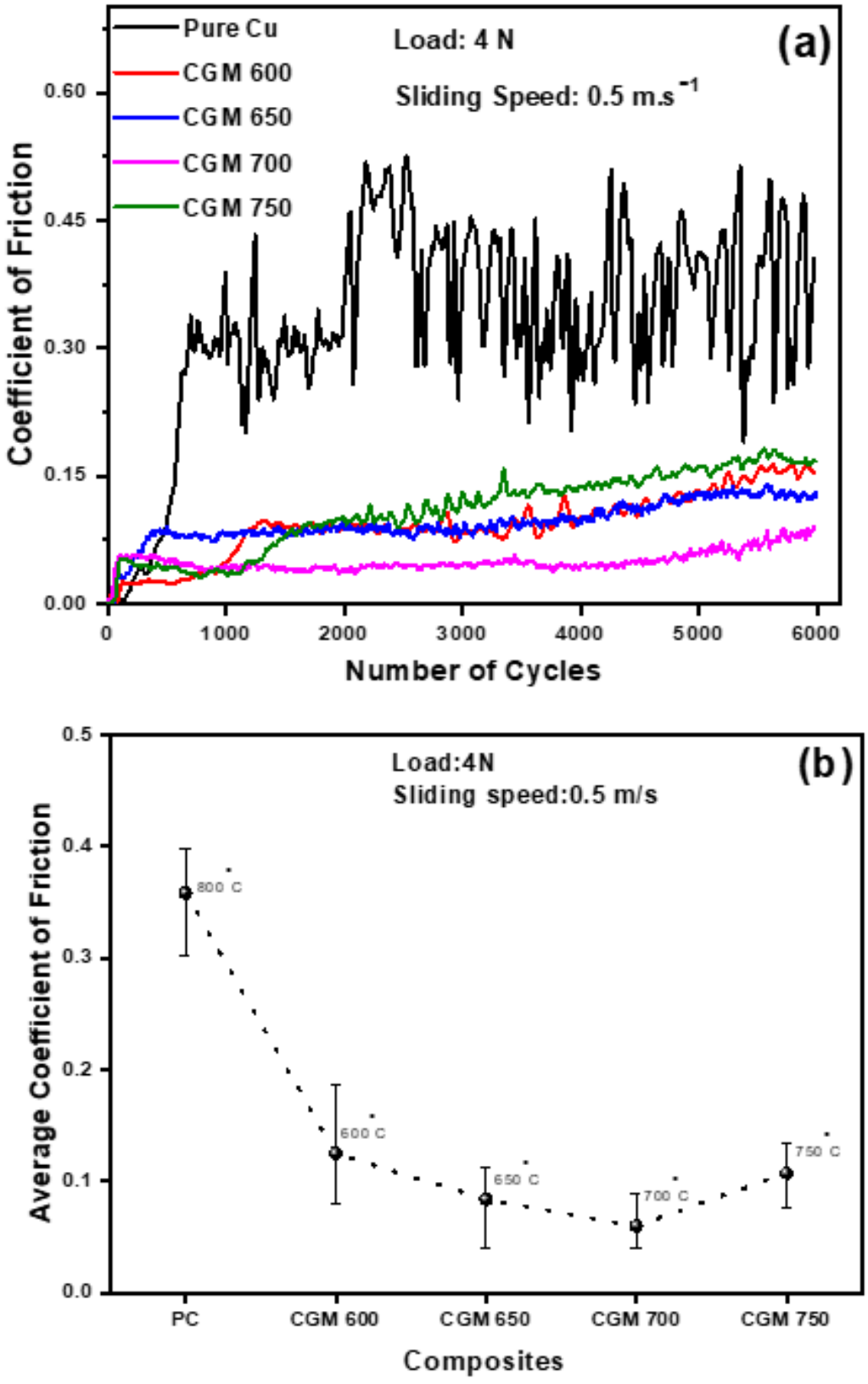

Fig. 5.14 (a) Variation of coefficient of friction with number of cycles, and (b) average coefficient of friction for PC and composites sintered at different sintering temperatures.

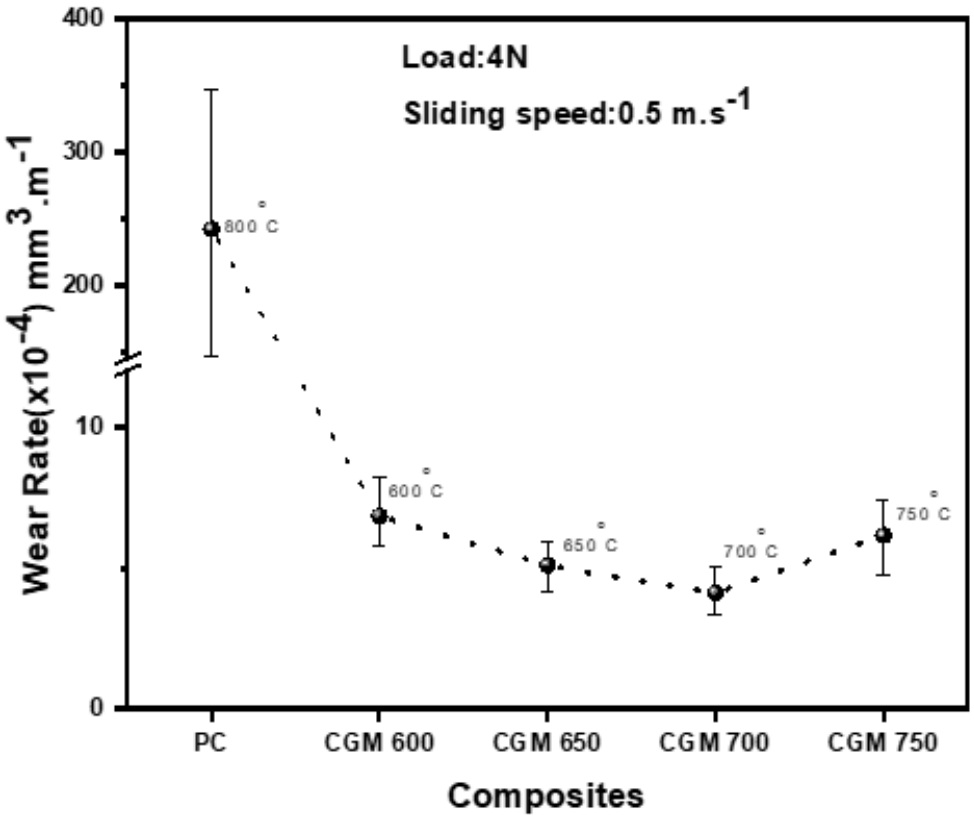

Fig. 5.15 Variation of wear rate of pure copper and Cu-rGO-MoS_2 composites.

From the forgoing results on the mechanical and tribological characterization, one may infer that CGM 700 has demonstrated optimum mechanical and tribological properties. Hence, the friction and wear performance of CGM 700 has further been evaluated at different loads of 4, 6, 8, and 10 N and fixed speed of 0.5 $m.s^{-1}$. The specimen of pure copper (PC) has also been tested under similar conditions for the purpose of comparison. Figure 5.16 (a) shows the variation of coefficient of friction with number of cycles at different loads (4, 6, 8, and 10 N) for PC and CGM700 composite. At a particular load, the real time variation of coefficient of friction with cycles represents fluctuating and continuously increasing trend for pure Cu (PC). However, the amplitude of fluctuations is relatively large at the lowest load of 4 N in comparison to other loads. In contrast, the composite CGM 700 has a relatively stable variation with significantly reduced amplitude of fluctuations at all the loads in comparison to that observed for PC.

However, the amplitude of fluctuations in CGM 700 is relatively large at a load of 10 N in comparison to other loads. Also, CGM 700 composite has shown a consistently lower coefficient of friction in comparison to PC at all the loads used in the present study. Figure. 5.16 (b) illustrates the variation of average coefficient of friction with respect to load for both PC and CGM 700. The average coefficient of friction has been found to increase with increasing load for pure Cu (PC), whereas the same for CGM700 is found to increase from 4 to 6N and remains almost constant thereafter, as evident from Fig. 5.16 (b). However, the average coefficient of friction is significantly lower for CGM 700 in comparison to that for PC at all the loads. A minimum value of the average coefficient of friction (~ 0.06) for CGM 700 has been observed at the lowest load of 4 N used in the present study.

Figure 5.17 shows the variation of wear rate with load for both pure Cu (PC) and CGM 700 composite. The wear rate is found to increase with increasing load for pure Cu whereas for CGM 700, it is observed to decrease slightly as the load increased from 4 N to 8 N which is followed by a sharp increase as the load is further raised to 10 N. However, CGM 700 containing 2 wt. % rGO-MoS_2 has shown a significantly lower wear rate in comparison PC at all the loads used in the present investigation.

The worn tracks of CGM 600, CGM 650, CGM 700, and CGM 750 have been examined under atomic force microscope (AFM), and the respective topographic images are presented in Figs. 5.18 (a through d). The peak-to-peak roughness on worn tracks of Cu-rGO-MoS_2 composites is found to be in the range of 1.14-2.5 µm. The worn tracks of the pure Cu (PC) could not be analyzed under AFM measurements due to being extremely rough. Hence, the roughness of the worn tracks of PC has been measured using an optical profilometer, and the same has been found to be (~20.8 µm), which is significantly higher in comparison to composites. Among all samples, Cu-rGO-MoS_2 composite CGM700

prepared at 700 ˚C sintering temperature has the minimum peak-to-peak roughness on the worn track of 1.14 µm.

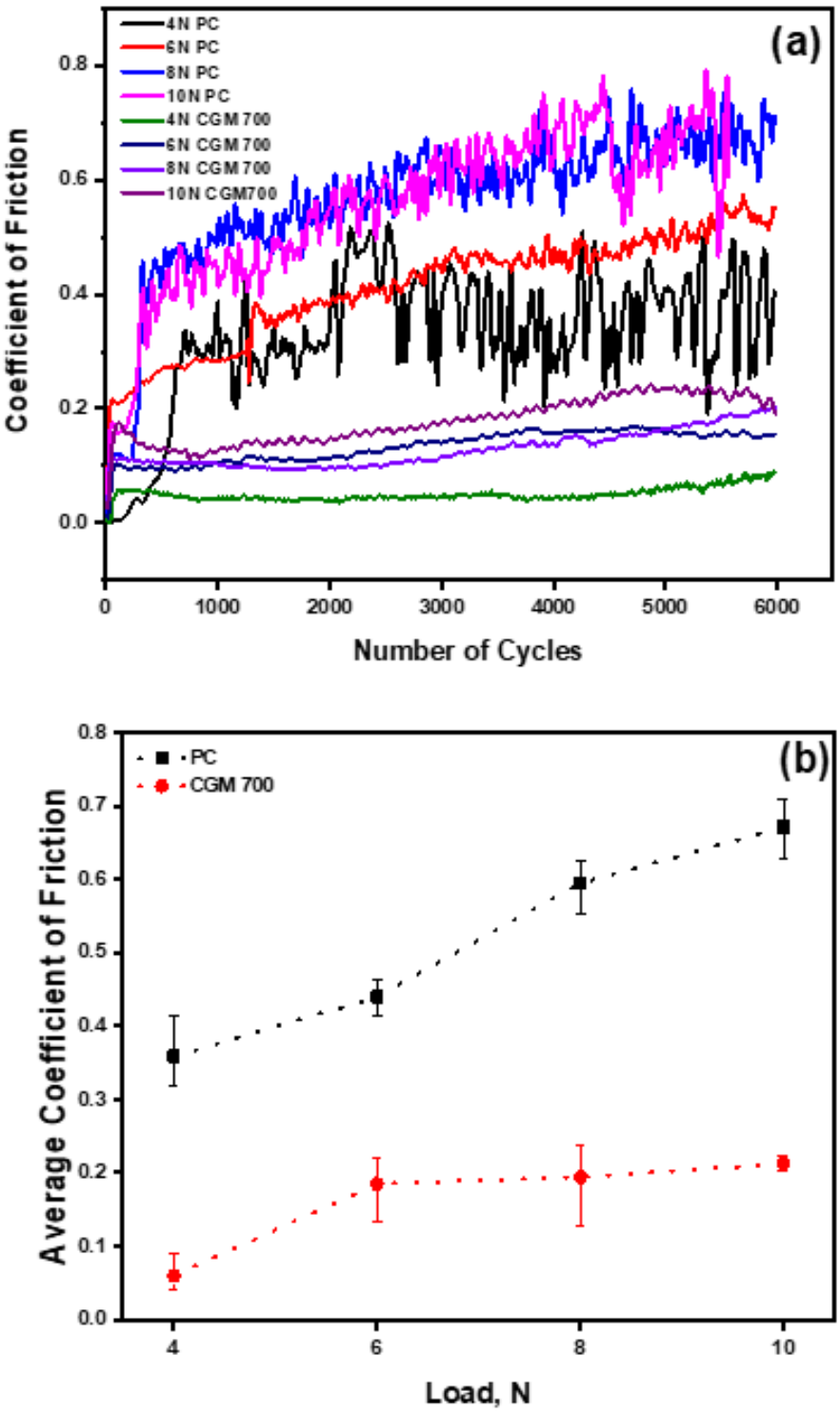

Fig. 5.16 (a) Variation of coefficient of friction with number of cycles, and (b) average coefficient of friction with load.

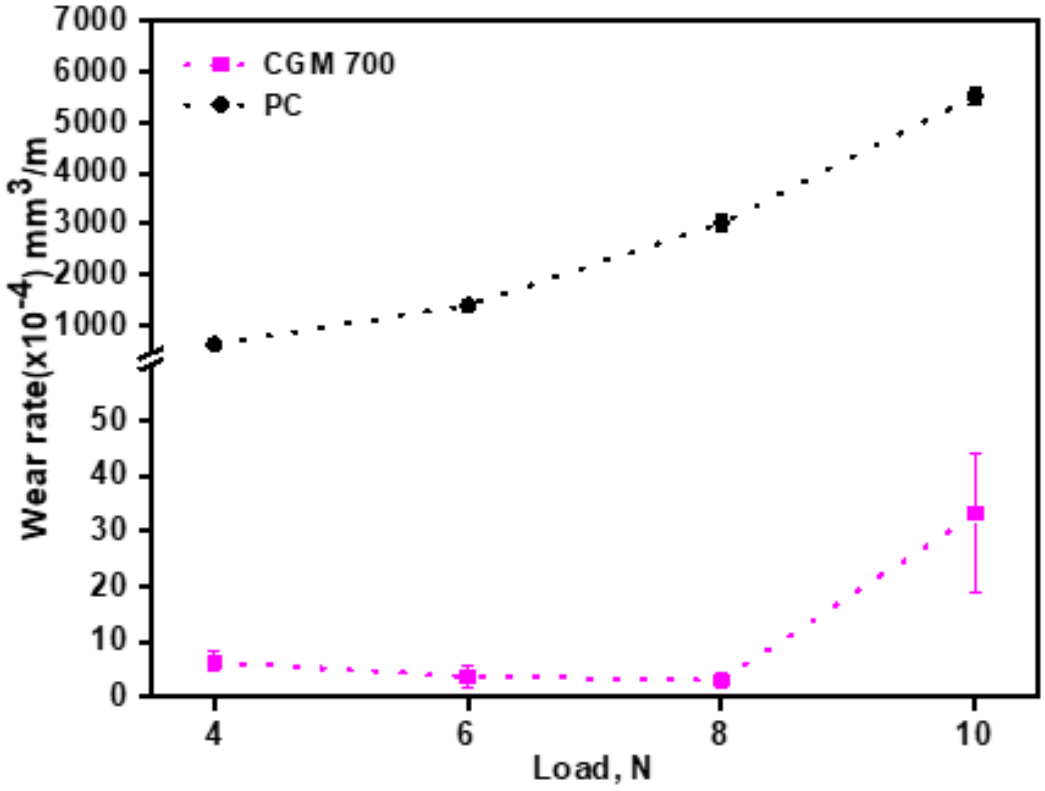

Fig. 5.17 Variation of wear rate with load for pure copper and optimized specimen.

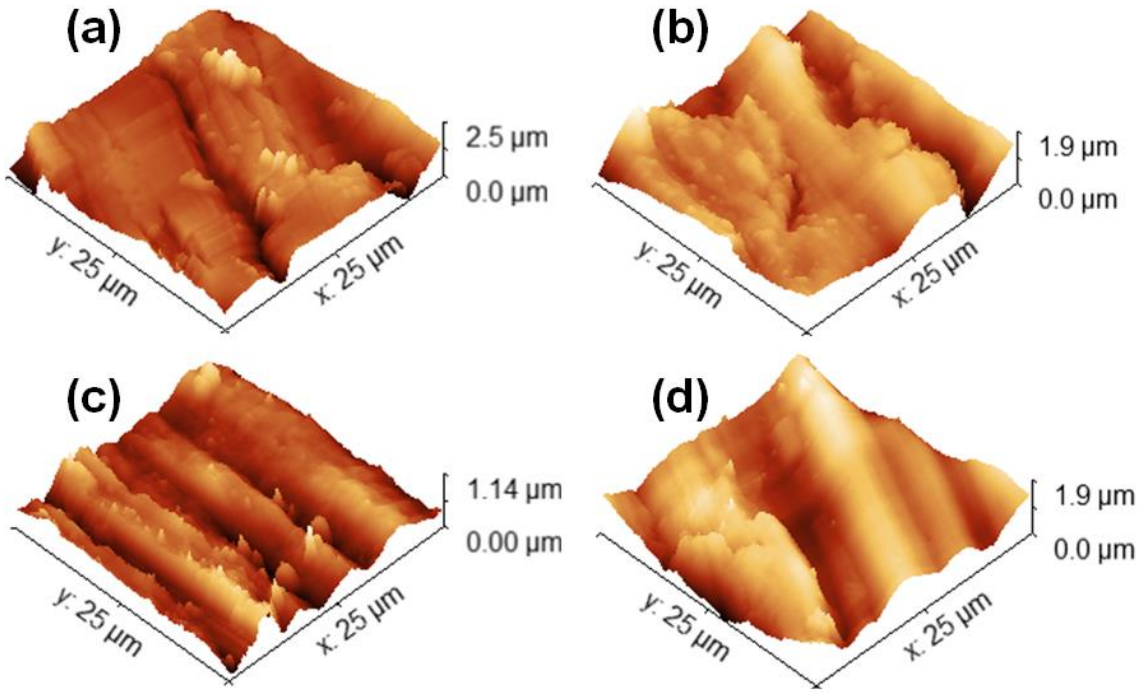

Fig. 5.18 The topographic images obtained from AFM of worn surfaces for (a) CGM 600, (b) CGM 650, (c) CGM 700, and (d) CGM 750 samples of Cu-rGO-MoS_2 composites after the tribo-test, tested under the load: 4 N, sliding speed: 0.5 m.s^{-1}.

The worn surfaces of PC and Cu-rGO-MoS_2 composites (CGM 600, CGM 650, CGM 700, and CGM 750) slid under a load of 4 N at a sliding speed of 0.5 $m.s^{-1}$ have been examined under SEM to explore the prevailing mechanisms of wear. The worn surface of PC presented in Fig. 5.19 (a) shows a severely deformed surface along with ploughing and adhesion assisted delamination at a few locations. However, adhesion, ploughing and tribo-film formation are observed to be the major wear events for composites sintered at different sintering temperatures as evident from SEM micrographs of the worn surfaces of composites given in Figs. 5.19 (b through e). However, the severity of ploughing and adhesion appears to reduce with an increase in sintering temperature from 600 to 700 $^{\circ}$C, as evident from a comparison of Figs. 5.19 (b), (c) and (d) corresponding to the composites CGM 600, CGM 650 and CGM 700. However, one may observe an increase in ploughing and adhesion effects for the composite CGM 750 sintered at 750 $^{\circ}$C as seen from Fig. 5.19 (e). The extent of tribo-film formation and the coverage provided by this film to the underlying substrate appears to be increasing as one moves from CGM 600 to CGM 700 followed by a marginal reduction for CGM 750, which may be judged from a comparison of Figs. 5.19 (b), (c), (d) and (e). EDS analysis of the selected area of the region containing the tribo-film and indicated by the white box in Fig.5.19 (d) suggests that the tribo-layer is rich in oxides and carbon and has low percentages of Mo, S elements.

Figures 5.20 and 5.21 show the worn scar area as examined under SEM and elemental mapping of the corresponding area for composites sintered at different temperatures. Figure 5.20 shows SEM images of worn scars on steel balls at low and high resolutions. The wear scar area has been observed to decrease with increasing sintering temperature from 600 to 700 $^{\circ}$C, beyond which it increases as evident from a comparison of Figs. 5.20 (a, c, e, and g) corresponding to the composites CGM 600, CGM

650, CGM 700 and CGM 750, respectively. The steel ball slid against Cu-rGO-MoS_2 composite CGM 700 exhibits the smallest wear scar compared to the balls slid against CGM 600, CGM 650, and CGM 750 composites, which may be judged from a comparison of Figs. 5.20 (a, c, e, and g). Figure 5.20 (a) and (b) show the wear scar corresponding to the counterface slid against the composite CGM 600 having a diameter of 469 µm, high magnification micrograph reveals the high abrasion features accompanied by the tribo-layer formation and simultaneous peeling off the tribolayer at some sites are observed. Elemental overlay explicitly shows the low coverage area of tribo-film formation over the counterface worn scar corresponding to the composite CGM 600. Worn scar developed on the steel ball counterface corresponding to CGM 650 is shown in Fig. 5.20 (c and d), low magnification image reveals that it is elliptical in shape having the major and minor axis dimensions as 591 µm and 380 µm, high magnification image shows the abrasive marks along with the tribo-layer presence, however, no signs of tribo-layer peeling are observed. Elemental overlay of CGM 650 counterface worn scar shows the low coverage area of tribo-layer formation, nevertheless, all the elements can be observed to be well dispersed over the tribo-layer region, which is found to be missing in the case of CGM 600. Low and high magnification micrographs of the worn surface corresponding to steel ball counterface slid against the CGM 700 composite is shown in Fig. 5.20 (e and f), diameter of circular shaped worn scar is 435 µm, high magnification image explicitly shows the less number of abrasive marks as compared to CGM 600 and CGM 650 counterface worn scar. Moreover, tribo-layer features are observed to be very pronounced compared to previous cases. High coverage area for tribo-layer is indicated by an elemental overlay, which seems to have better elemental distribution. Figure 5.20 (g and h) refers to the low and high magnification micrograph of counterface slid against the composite CGM 750, a worn elliptical scar of 613 µm major axis diameter and 402

μm minor axis diameter is obtained, abrasive marks are observed along with tribo-layer peeling at several sites in high magnification micrograph. However, elemental overlay indicates a moderate amount of area coverage by tribo-film with good dispersion of elements.

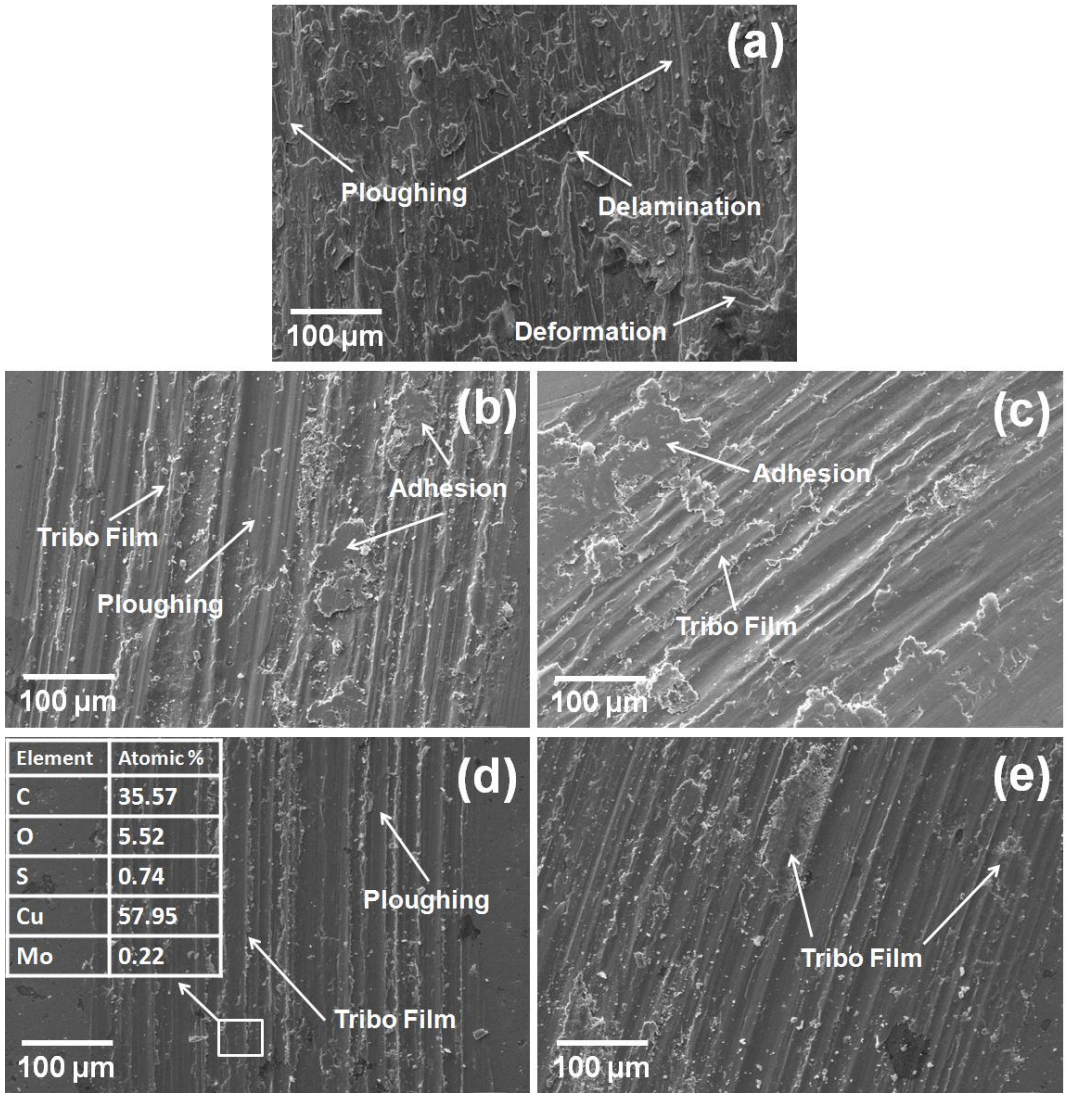

Fig. 5.19 Worn surface micrographs depicting the wear events for the specimens (a) PC, (b) CGM 600, (c) CGM 650, (d) CGM 700, and (e) CGM 750, tested under the load of 4N and 0.5 $m.s^{-1}$.

Figure 5.21 demonstrates SEM micrographs and the corresponding elemental distribution of worn scars on steel balls slid against different composites. The Mo, S, and C are observed to be thoroughly distributed on the worn surfaces of steel balls indicating

the transfer of rGO-MoS_2 hybrid from the Cu-rGO-MoS_2 composite to the ball surface. Besides that, the copper is also found to be transferred in the form of strips along the sliding direction, which is further supported by elemental overlay images shown in Figure 5.20. The relatively uniform distribution of Mo, S, and C, which are the constituent elements of rGO-MoS_2 hybrid, formed the tribo-interactive thin film on the counter steel balls. Nevertheless, distribution is observed to be more uniform in the case of CGM 700, as observed from the elemental overlay and elemental distribution shown in Figs. 5.20 and 5.21.

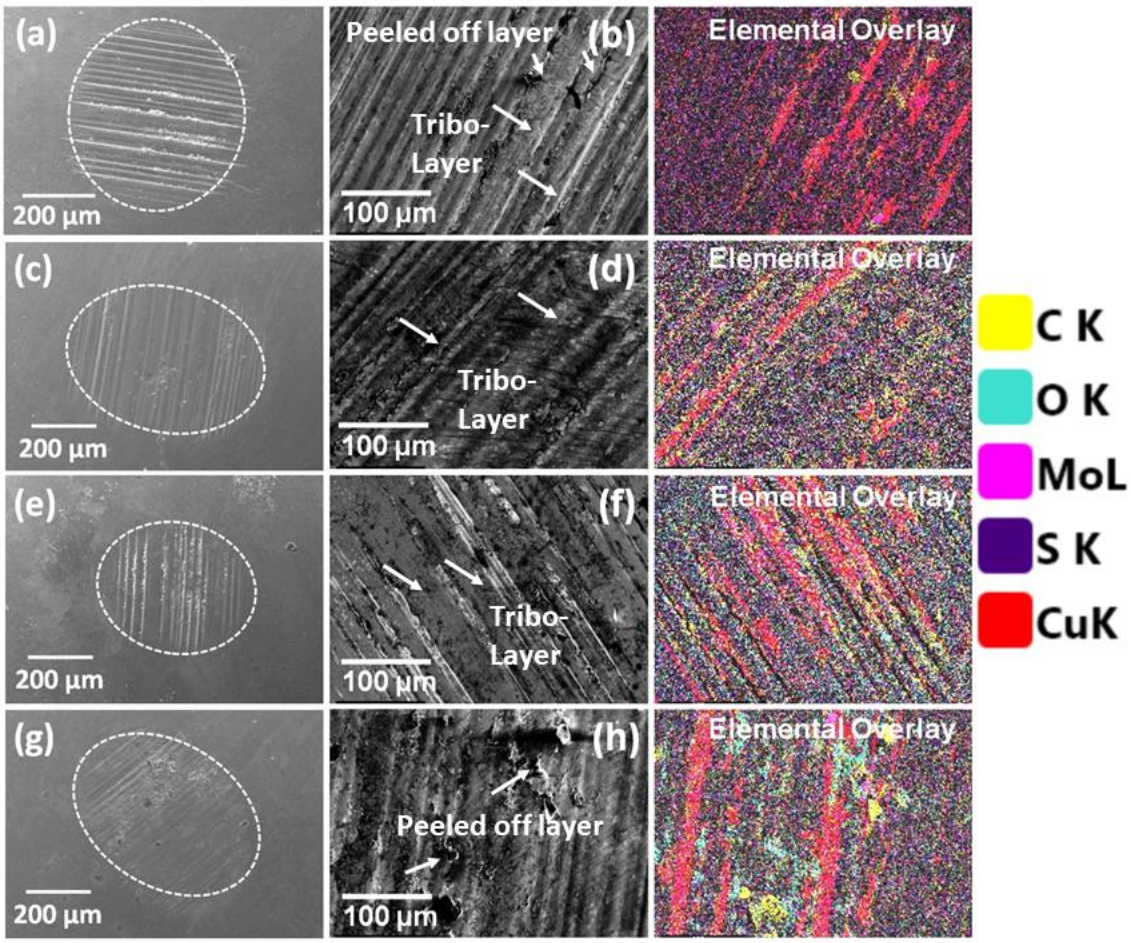

Fig. 5.20 SEM Micrographs of counter surface steel balls slid against (a-b) CGM 600, (c-d) CGM 650, (e-f) CGM 700, and (g-h) CGM 750 samples of Cu-rGO-MoS_2 composites. The FESEM micrographs at higher resolutions are shown with corresponding elemental distribution overlay obtained from EDAX.

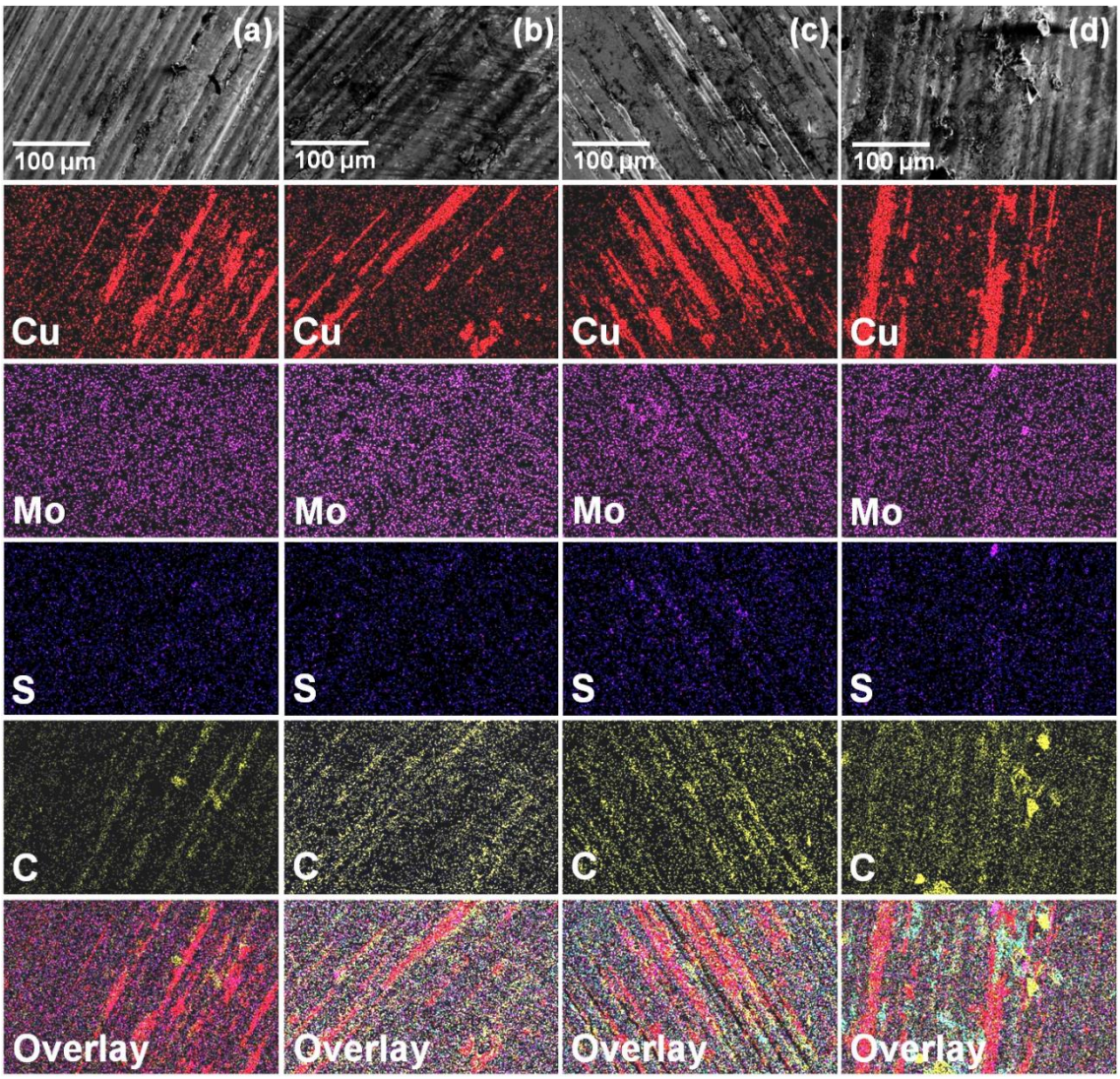

Fig. 5.21 Micrographs of worn scars developed on steel balls during tribo-tests against (a) CGM 600, (b) CGM 650, (c) CGM 700, and (d) CGM 750 samples of Cu-rGO-MoS_2 composites. The SEM micrographs are shown along with corresponding area elemental distribution and overlay of all contributing elements.

Figures 5.22 (a) and (b) show the SEM micrographs of the worn surfaces of PC and CGM 700, respectively, after being slid at the highest load of 10 N used in the present study. The worn track shown in 5.22 (a) corresponds to the specimen PC tested at 10N load, it is evident from the micrograph that abrasion is the major wear mechanism that is accompanied by ploughing and minor adhesion. Whereas, tribo layer formation and abrasion are the major wear events accompanied by minor adhesion, observed for composite CGM 700.

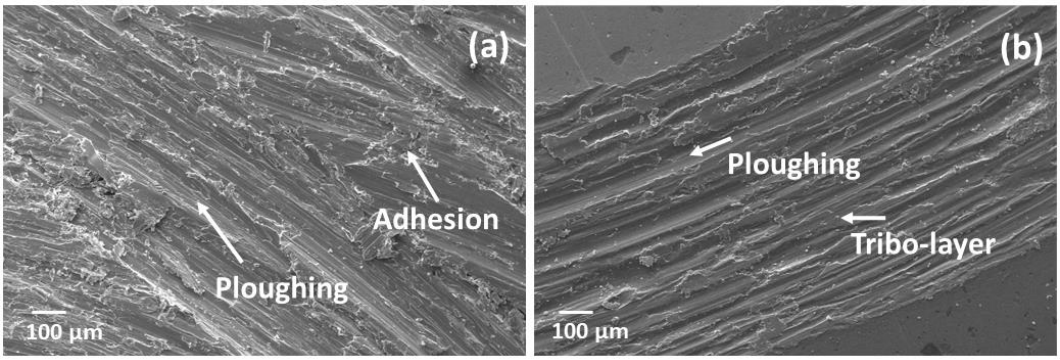

Fig. 5.22 Scanning electron micrographs of worn tracks developed on (a) PC and (b) CGM 700 composite under the load of 10 N at sliding speed of 0.5 $m.s^{-1}$ sliding speed.

5.2 DISCUSSION

The characteristics diffraction features at 2θ of 13.9, 33.3, 39.3, and 58.9° corresponding to the (002), (101), (103), and (110) planes of MoS_2 nanosheets observed in the XRD pattern of rGO-MoS_2 hybrid shown in Fig. 5.4 exhibits are in consonance with the findings of Ding et al., (2012) . Also, the presence of comparatively weak and broad diffraction peaks in Fig. 5.4 at 2θ of 24.8° corresponding to the (002) plane of rGO confirms the preparation of rGO-MoS_2 hybrid, which is shown in Fig. 5.2. The presence of characteristics D and G bands in the first-order Raman spectrum of rGO-MoS_2 hybrid given in Fig. 5.5 reveals the presence of structural defects and sp^2 carbon domains, respectively, in the graphene skeleton. This may be attributed to the elimination of a major fraction of oxygen functionalities in the GO and the formation of rGO during the hydrothermal treatment, as indicated by Choudhary (2013). Simultaneously, the structural defects and residual oxygen functionalities also act as active sites for the growth of MoS_2 nanosheets on the surface of rGO under the hydrothermal reaction. The higher intensity ratio (I_D:I_G = 1.39) between the D and G bands (Fig. 5.5) indicates the existence of structural defects and distortions in the graphene lamellae of rGO-MoS_2 hybrid. The

presence of MoS_2 has been confirmed by characteristic A_{1g} band at 403 cm^{-1} shown in the inset of Fig. 5.5. The E^1_{2g} mode of MoS_2 usually disappears in the suspended material due to the breaking of symmetry by interaction with rGO lamellae in the rGO-MoS_2 hybrid, which has also been reported earlier by Hajiyev, (2013). The HRTEM micrographs illustrated in Figs. 5.2 (a and b) explicitly demonstrate that MoS_2 nanosheets and ribbon-like structures of MoS_2 lamellae are homogeneously grown on the rGO skeleton. The uniform distribution of Mo and S beside the C in rGO-MoS_2 hybrid further confirms the homogeneous distribution of MoS_2 nanosheets in the rGO-MoS_2 hybrid, as evident from TEM image of the rGO-MoS_2 hybrid and the corresponding area elemental distribution of Mo, S, and C given on Fig. 5.2 (c). The weak shoulder of Mo 3d at a higher binding energy of 236.3 eV shown in the XPS survey spectrum of rGO-MoS_2 hybrid (Fig. 2) assigned to Mo (VI) oxidation state may be attributed to the presence of traces of MoO_3 in rGO-MoS_2 hybrid. It has been indicated by Liang et al. (2011) that Mo sites, available primarily at the edges and defect sites are prone to oxidation, which results in the formation of MoO_3. In the present study, the availability of residual oxygen functionalities in the rGO might have facilitated the oxidation of lower-coordinated sites of Mo at the edges, resulting in the generation of MoO_3 traces in rGO-MoS_2 hybrid.

The microstructure of Cu-rGO-MoS_2 composites prepared at different sintering temperatures and given in Figs. 5.6 (a through d) reveals an almost uniform distribution of rGO-MoS_2 hybrid in the copper matrix with some carbon rich darker areas and MoS_2 rich light grey regions, which reflects a thorough blending of rGO-MoS_2 hybrid *via* multidimensional interactions with the copper matrix. The lack of distinct boundaries between the rGO-MoS_2 hybrid and copper matrix, as seen in Fig. 5.7 (b) also confirms the occurrence of multidimensional interactions or linkages between them, which is very important for good quality reinforcement.

The diffraction peak at 2θ of 26.5 degrees owing to (002) plane shown in XRD pattern of composites depicted in Fig. 8 confirms the presence of rGO and the presence of a broad peak at 2θ of 33.4-degree corresponding to (101) plane suggests the participation of MoS_2 in the Cu-rGO-MoS_2 composites. The emergence of a new diffraction peak at 2θ of 36.4 degrees corresponding molybdenum carbide, MoC, may be attributed to the interaction between rGO and MoS_2 facilitated by high temperature and pressure sintering leading to the formation MoC as reported by Kumar et al. (2018). The extraordinary hardness of MoC is expected to be beneficial for the hardening of Cu-rGO-MoS_2 composites and their potential for wear protection and load-bearing capability.

The first order Raman spectra of Cu-rGO-MoS_2 composites and the intensity ratio of D and G bands (I_D/I_G) given in Fig. 9 (a) suggests the presence of structural defects and sp^3 carbon in graphitic domains of Cu-rGO-MoS_2 composites. The intensity ratio of D and G bands in the rGO-MoS_2 hybrid (I_D/I_G = 1.39, Fig. 5.5) is noted to be higher than the Cu-rGO-MoS_2 composites (I_D/I_G = 1.19-1.21, Fig. 9 a) which suggests that rGO-MoS_2 hybrid carries a larger degree of disorderness owing to residual oxygen functionalities and structural defects in the graphene skeleton. A decrease in I_D/I_G ratio may be attributed to the elimination of residual oxygen functionalities during ball-milling and high temperature sintering processes which might have healed the structural defects of rGO to some extent and resulted in a lower I_D/I_G ratio in Cu-rGO-MoS_2 composites

A shift in G band position as a function of sintering temperature illustrated in Fig. 9 (b) could be explained on the basis of the anharmonic coupling of the phonon modes and the thermal expansion of the materials as suggested by (Calizo et al., 2007 and Costa et al., 2015). The thermal responses of rGO, Cu, and MoS_2 components in Cu-rGO-MoS_2 composites and changes in volume driven by different sintering temperatures

collectively generate anharmonicity in graphene skeleton of rGO, leading to a shift in G band. The Cu, MoS_2, and rGO as constituent materials of Cu-rGO-MoS_2 composites have different coefficients of thermal expansion; graphene shows the negative coefficient of thermal expansion, whereas Cu and MoS_2 exhibit positive coefficients of thermal expansion Yoon et al. (2011) and Zhang et al. (2016). The disparity in coefficients of thermal expansion of Cu, MoS_2, and rGO leads to strain in graphene sheets of Cu-rGO-MoS_2 composites. The increase of Raman shift suggests the in-plane contraction of graphene, while a decrease indicates the in-plane expansion (Yoon et al., 2011). The shifting of G band position towards left (known as redshift) with increasing sintering temperature from 600 to 700 $^{\circ}$C in composites CGM 600, CGM 650, and CGM 700 indicates an in-plane expansion of graphene sheets in the Cu-rGO-MoS_2 composites. The blue-shift of the G band observed with an increase in sintering temperature from 700 to 750 $^{\circ}$C (Fig. 9 b) may be ascribed to the contraction of graphene sheet in Cu-rGO-MoS_2 composite.

The density, hardness, and ultimate tensile strength (UTS) have been found to decrease with increasing sintering temperature, as observed from Table 5.1 and Figs. 5.11 and 5.12. A gradual decrease in density of Cu-rGO-MoS_2 composites with increasing sintering temperature is attributed to volume expansion caused by the different thermal expansion coefficients for Cu, MoS_2 (positive), and rGO (negative). The higher sintering temperature facilitates the diffusion of low melting components leading to the generation of porosity. The occurrence of such events increases with increasing sintering temperature resulting in a gradual reduction in density. The difference in coefficient of thermal expansion of constituent components also plays a significant role in governing the punch displacement and hence, the density. As seen in Fig. 5.10, the punch displacement increases with increasing sintering temperature and reaches a plateau at ~ 400 $^{\circ}$C. A

decrease in punch displacement beyond 400 ˚C reflects an increase in volume, which further confirms the reduction in the density at relatively higher sintering temperatures. This may be attributed to the different thermal expansion coefficients of constituent components in Cu-rGO-MoS_2 composites. The copper and MoS_2 have positive thermal expansion, while graphene exhibits negative thermal expansion, as reported by Yoon et al. (2011) and Zhang et al. (2016). The expansion of copper and MoS_2 and the contraction of graphene result in the generation of porosity leading to a gradual decrease in the punch displacement beyond 400 ˚C. Significantly higher hardness of Cu-rGO-MoS_2 composites compared to pure copper may be explained on the basis of the restriction to the movement of the dislocations offered by the uniformly dispersed rGO-MoS_2 hybrid in the copper matrix. Interestingly, the hardness of Cu-rGO-MoS_2 composites is observed to decrease marginally with increasing sintering temperature, and it could be attributed to the gradual reduction in the densification at relatively higher sintering temperatures, as explained earlier. The other contributing factor may the difference in the distribution of the reinforced phase in the matrix that occurs with the increasing temperature of sintering. One may observe from the microstructures of the composites shown in Fig. 5.6 (a through d) that despite the distribution is almost uniform at a relatively lower temperature of sintering as seen from a well distributed carbon rich and MoS_2 rich regions (Fig. 5.6 a) which are relatively fine in size in comparison to those seen in Figs. 5.6 (b, c, and d), which show an increase in size as well as clustering with increasing temperature of sintering. This may also explain a decrease in the tensile strength of composites with increasing temperature of sintering as observed stress-strain curves given in Fig. 5.12, and Table 5.1. The observed behavior may also be explained on the basis of the fractographs and their respective elemental mapping shown in Fig. 5.13 for all the composites sintered at different temperatures. It can be deduced from the elemental mapping of the fractographs that reinforcement phase is more uniformly distributed over

the fractured surface of the composites sintered at relatively low temperatures, whereas the reinforcement phase is agglomerated in the case of composites sintered at high temperature. The presence of a dispersed reinforcement phase over the fractured surface indicates the effective load transfer between copper and rGO-MoS_2 in composite sintered at relatively low temperatures. However, the particle pull-out observed in the case of a fractured surface of composites sintered at relatively high temperatures reflects the loss of load transfer efficiency between the matrix and the second phase.

The variation of friction coefficient with number of cycles for PC as well as composites synthesized at different sintering temperatures, i.e., CGM 600, CGM 650, CGM 700, and CGM 750 during testing at a load of 4 N and sliding speed of 0.5 $m.s^{-1}$ shown in Fig. 5.14 (a) depicts the fluctuating trend. The occurrence of a fluctuating trend may be attributed to the variation in the contact when the specimen and the counterface are evolving to develop better surface conformity. However, the amplitude of fluctuations is significantly large for PC in comparison to comparison to composites, which show a stable variable with reduced amplitude of fluctuations. The difference in behavior may be explained on the basis of the SEM micrographs of the worn surface of specimens as well as counterface ball illustrated in Figs.5.19 and 5.20. The larger fluctuations observed for PC may be attributed to the severe plastic deformation, as shown in Fig. 5.19 (a) and the occurrence of metal-metal contact between the specimen and the counterface steel ball. This may also explain a higher average coefficient of friction and high wear rate for PC in comparison to that for the composites, as evident from Fig. 5.14 (b) and Fig. 5.15. However, a stable variation with significantly low coefficient of friction and low wear rate for composites may be attributed to the formation and existence of a tribo-layer over the worn track of the composites and that of a transfer layer over the counter face steel ball for composites CGM 600, CGM 650, CGM 700 and CGM 750 as observed in Figs.

5.19 (b, c, d, and e) and 5.20 (b, d, f, and h). One may observe the similar trend of average coefficient of friction and wear rate obtained for the composites from Fig. 5.14 (b) and Fig. 5.15, which clearly indicates that friction and wear can be explained by a single operating mechanism. The elemental distribution of the tribo-layer given in Fig. 5.21 also confirms the presence of solid lubricants. The presence of tribolayer avoids the metal-metal contact between specimen and counterface ball while simultaneously providing a low shearing capability at the sliding interface. Both of these events lead to a reduction in the coefficient of friction and loss of material due to wear. One may observe that the average coefficient of friction and wear rate decreases with increasing sintering temperature till 700 $^{\circ}$C corresponding to CGM 700 and increases thereafter for the composites CGM 750 sintered at 750 $^{\circ}$C. The values obtained for average friction coefficient and wear rate of composites may be explained on the basis of the presence of the tribo-layer and its extent of coverage over the surface along with the uniformity. The tribo-layer appears to cover a relatively larger area of the surface for CGM 700 (Fig. 5.19 d) in comparison to other composites and appears to be more uniform whereas the layer appears to have fractured at few locations (Fig. 5.19 b, c), which have been supported by the AFM micrograph shown in Fig. 5.18. It can be seen clearly from AFM micrograph of worn surface of composites that grooves become shallow and less wide for higher sintering temperature composite till 700 $^{\circ}$C and becomes deeper and wider on increasing the temperature to 750 $^{\circ}$C. The groove area in the AFM micrograph indicates the penetration of tribo-layer from the asperities, while the upland area represents the tribo-layer formation. Tribo-layer formed over the worn surface consists of Cu, Mo, S, C, and O, as observed from EDX analysis reflecting, thus, the presence of graphene and MoS_2, which might have facilitated the smooth sliding of steel ball over the surface, as observed from Fig. 5.19 (c). The elemental distribution and wear events of steel ball counterface slid against composites shown in Fig**.** 5.20 and 5.21 indicate the transfer of material from

the composite disc to the steel ball surface. The Mo, S, and C are found to be thoroughly distributed on the worn surfaces of steel balls, which reveals the transfer of rGO-MoS_2. The Cu is also found to be transferred in the form of strips in sliding directions, as supported by elemental overlay in Fig. 5.21. These results suggest that copper matrix wears out and some of the worn material get transferred and adhered to the contact interface of steel balls, driven by tribo- stress. Area of the worn scar also indicates the severity of wear and magnitude of friction coefficient, as it is also the measure of area of metal to metal contact. The MoS_2 in rGO-MoS_2 carries dangling sulfur sites that interact with iron and form a protective thin film as reported by Kumari et al. (2016). Simultaneously, rGO having structural defects also has a good affinity towards iron, which helps it to get adhered to the steel surface (Chouhan et al., 2018). The uniform distribution of Mo, S, and C on the worn surface of steel balls, as seen from Fig. 5.21 supports the formation of rGO-MoS_2-based tribo thin film. The weak van der Waals interaction between atomic/molecular lamellae of rGO and MoS_2 in rGO-MoS_2 hybrid results in low resistance to shear and leads to a reduction in friction in Cu-rGO-MoS_2 composites under the sliding tribo-stress, smooth sliding of counterface over the composite inhibits the wear loss. The presence of rGO-MoS_2 hybrid in the Cu-rGO-MoS_2 composites and the transfer of rGO and MoS_2 containing hybrid thin film on counter steel balls facilitate the sliding events. The tribo-layer formation over the surface of both the mating bodies inhibits the metal-metal contact and results in a reduced coefficient of friction and low wear rate. A relatively higher wear rate for pure copper compared to the composites could also be explained on the basis of the hardness. It has been indicated by Archard (J.F Archard, 1953) that the hardness is inversely proportional to wear rate. Hence, it is not surprising that the Cu having a relatively lower hardness in comparison to composites has a higher wear rate, as seen in Fig. 5.15. Among the composites, the wear rate shown by the composite CGM 600 is the highest despite its higher hardness in

comparison to other composites, which indicates that hardness is not the sole factor in dictating the wear behavior. The other aspects like presence of tribo-layer, its detachment, and the extent of cover over the sliding surface also play a crucial role in governing the wear process under dry sliding. The tribo-layer is observed to cover a larger extent of the worn surface for CGM 700 in comparison to other composites, as evident from a comparison of Figs. 5.19 (b, c, d, and e), which is able to inhibit the metal-metal contact in an effective manner and leads to a reduction in wear, as explained earlier also. Hence, CGM 700 has the least wear rate despite its relatively lower hardness in comparison to CGM600 and CGM650 due to the relatively lower extent of coverage provided by the tribo-layer as well as the detachment of the of this layer at a few locations in these composites as observed in Figs. 5.19 (b and c).

Based on the results and their discussion presented above, it may be concluded that the composite CGM 700 sintered at 700 $^{\circ}$C has shown the optimum performance. Since, normal load plays an important role in controlling and affecting the tribo-events, the friction and wear characteristics of CGM 700 have been examined under different loads of 4, 6, 8 and 10 N. An unstable and fluctuating (with relatively large amplitude) variation of coefficient of friction for pure copper (PC) in comparison to that for CGM 700 at all the loads used in the present study may again be attributed to the occurrence of metal-metal contact between PC and steel ball also evident from Figs. 5.19 (a) and 5.22 (a) and the avoidance of the same in CGM 700 due to presence of tribo-layer over the worn surface (Figs. 5.19 d and 5.22 b). The increase in average coefficient of friction with increasing normal load in PC may be attributed to the increase in load which results in greater digging of asperities of the harder counterface ball into the soft Cu and leads to enhancement in the severity of abrasion with increasing load which could be confirmed by the comparison of SEM micrographs (Figs. 5.19 (a) and 5.22 (a)) of the

surfaces worn under loads of 4 and 10 N, respectively. This may also explain an increase in wear rate in PC with increasing load and a relatively larger wear rate in comparison to CGM 700 at all the loads, as observed in Fig. 5.17. A relatively lower hardness of PC as compared to CGM 700 might also have resulted in a higher wear rate in PC as it is an accepted fact that harder the material better is the resistance to wear. A significantly lower coefficient of friction in CGM 700 in comparison to PC at all the loads could be ascribed to the presence of a tribo-layer containing lubricious compounds which provide low shearing ability at the interface between the mating bodies and avoids the metal-metal contact to some extent based on the applied load leading to lower friction as well as wear rate in the composite as explained earlier also. An increase in friction coefficient with increasing load in CGM 700 may be attributed to the possibility of penetration of the tribo-layer by the asperities of the counterface ball with increasing load. However, no measurable changes are observed in wear rate of CGM 700 composite with an increase in load from 4 to 8 N, and it has been observed to increase slightly at a load of 10 N (Fig. 5.17). The inherent lubricity by rGO-MoS_2 in CGM 700 composite and formation of rGO-MoS_2 containing tribo thin film on counter surface protects contact interface. As a result, Cu-rGO-MoS_2 composite shows no considerable changes in wear rate with increasing of the load from 4 to 8 N. An increase in wear rate as the load is raised from 8 N to 10 N (Fig. 5.17) may be attributed to the increased abrasion caused by an increased load as evident from the presence of deeper grooves shown in SEM micrograph given in Fig. 5.22 (b) and the penetration of tribo-film by counter face asperities giving rise to metal-metal contact resulting in loss of protection to underlying material provided by tribo-film.

The contraction and expansion in the Cu-rGO-MoS_2 composites are driven by temperature and strain, which are manifested by a shift in G band position as a function of sintering temperature shown in Fig. 5.9 (b). The G band shift is attributed to the

anharmonic coupling of the phonon modes and the thermal expansion of the material. The thermal responses of rGO, Cu, and MoS_2 components in Cu-rGO-MoS_2 composites and changes in volume driven by different sintering temperatures collectively generate anharmonicity in graphene skeleton of rGO, leading to a shift of G band. The disparity in coefficients of thermal expansion of Cu, MoS_2, and rGO leads to the generation of strain in graphene sheets in Cu-rGO-MoS_2 composites. The increase of Raman shift reflects the in-plane contraction of graphene, while a decrease indicates the in-plane expansion (Yoon et al., 2011). The lowering of G band position with increasing sintering temperature from 600 to 700 ˚C in composites CGM 600, CGM 650, and CGM 700 indicates in-plane expansion of graphene sheets in the Cu-rGO-MoS_2 composites. Furthermore, an increase in sintering temperature to 750 ˚C for CGM 750 composite represents a blue-shift of G band, which is associated with the contraction of graphene sheet in Cu-rGO-MoS_2 composite. The contraction and expansion in the graphene and other components (copper and MoS_2) influence the mechanical and tribological properties of resultant composites. To explain the probable mechanism, in-plane contraction and expansion are illustrated with the help of a schematic diagram given in Fig. 5.23. It demonstrates the pictorial view of graphene distribution in the copper matrix, which is compactly packed with each other as revealed by the microstructure of Cu-rGOMoS_2 composites shown in Fig. 5.6. During the tribo-test, the cyclic sliding-stress acts on the surface of Cu-rGO-MoS_2 composites and the constituent components, including rGO, experience in-plane cyclic compressive loading. It has been reported that graphene sheets are three times stronger in tension compared to compression and fail at a higher rate in case of in-plane axial compressive force due to buckling of graphene sheet leading to degradation of the properties (Androulidakis et al. 2015 and Yang et al., 2016). The Cu-rGO-MoS_2 composite CGM 600 prepared at 600 ˚C contains rGO sheets with compressive residual stress when it is subjected to sliding stress, which causes the failure of the graphene sheet. Thus the wear

rate and friction coefficient are higher compared to remaining composite samples CGM 650, CGM 700, CGM 750. A decrease in coefficient of friction and wear rate with increasing sintering temperature till 700 ˚C may be attributed to the expansion of graphene sheets which causes a decrease in cumulative compressive stress due to relatively higher sintering temperature and as a result, these composites are able to survive a higher number of cycles before wearing out. Further increase in temperature of sintering beyond 700 ˚C indicates a contraction of graphene sheet in the CGM 750 composite, which might have raised the coefficient of friction and wear rate in CGM 750 composite.

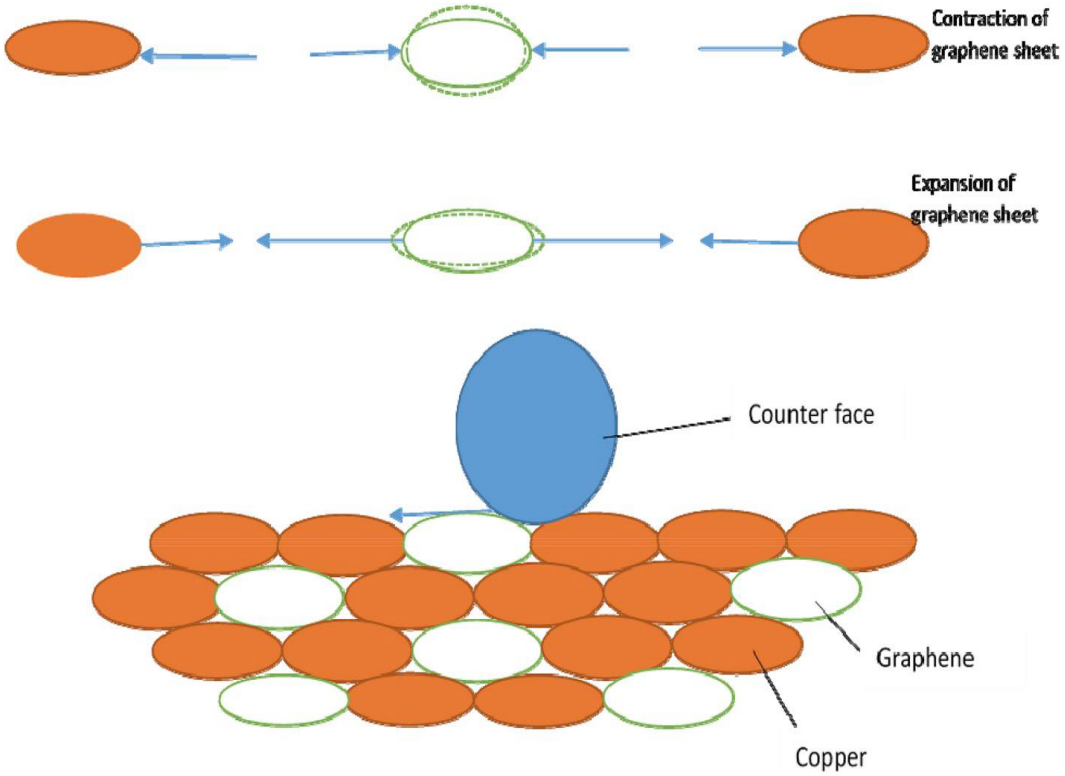

Fig. 5.23 Schematic illustration representing the sliding of counterface over the Cu-rGO-MoS_2 composite. It demonstrates the expansion and contraction of graphene sheets along with the nature of forces acting during the sliding.

Based on the results and discussion presented above, it can be inferred that Cu-rGO-MoS_2 composites reinforced by uniformly distributed rGO-MoS_2 hybrid, synthesized through a hydrothermal approach using GO as platform material to grow

MoS2 nanosheets, can be successfully prepared via spark plasma sintering at different temperatures. The addition of 2 wt. % rGO-MoS_2 hybrid results in a significant improvement in hardness and tensile strength of pure copper which has been attributed to (i) the uniform distribution of rGO-MoS_2 hybrid in the matrix, (ii) restrictions of dislocation movement by the second phase via multidimensional and (iii) the presence of hard MoC. The hardness and strength of Cu-rGO-MoS_2 composites change with sintering temperature from 600 to 750 $^{\circ}$C due to different coefficients of thermal expansion of the constituent materials. The addition of rGO-MoS_2 hybrid significantly reduces the coefficient of friction and wear rate and the magnitude reductions are found to be controlled by (i) microstructure and hardness of composites with increasing sintering temperature, (ii) the presence of a smooth tribo-layer over the worn surface and (iii) the transfer of rGO-MoS_2 to the counterface ball which facilitates the sliding by providing an easy shearing interface. The composite sintered at 700 $^{\circ}$C has shown the optimum tribological performance while maintaining a reasonable level of mechanical properties. A mechanism, based on the contraction and expansion of graphene skeleton in the Cu-rGO-MoS_2 composites as a function of sintering temperature and sliding stress has been proposed to explain the relative changes in the friction and wear behavior among the Cu-rGO-MoS_2 composites. The self-lubricating properties of rGO-MoS_2 hybrid in composites and formation of rGO-MoS_2 containing tribo-thin film on the counter surface are believed to have played vital roles in improving the tribological performance in terms of reduced friction and wear rate. Hence, it may be inferred that rGO-MoS_2 hybrid can be a promising and potential candidate for developing the Cu-based self-lubricating composites for various tribological applications.